Cell Reports

Article

The intrinsically disordered region of coronins fine-tunes oligomerization and actin polymerization

Graphical abstract

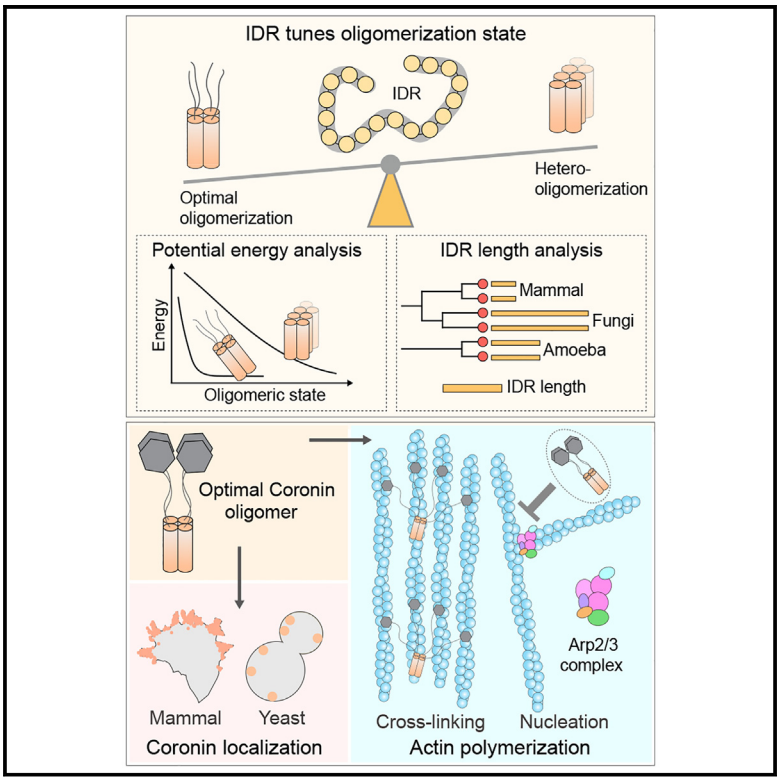

Highlights

- IDR fine-tunes coiled-coil-mediated protein oligomerization
- Oligomerization states determine coronin's biochemical activities and functions
- IDR's molecular grammar and length influence coronin oligomerization

Authors

Xiao Han, Zixin Hu, Wahyu Surya, ..., Jaume Torres, Lanyuan Lu, Yansong Miao

Correspondence

yansongm@ntu.edu.sg

In brief

Han et al. found that an intrinsically disordered region (IDR) optimizes coronin activity. The IDR fine-tunes the oligomerization of the neighboring coiled coil, maintaining coronins in a tetrameric state crucial for F-actin cross-linking and Arp2/3-mediated actin polymerization. Three factors contribute to coronin oligomerization: helix packing, coiled-coil energy landscape, and the IDR's length and sequence.

Han et al., 2023, Cell Reports *42*, 112594
June 27, 2023
https://doi.org/10.1016/j.celrep.2023.112594

CellPress

Cell Reports

CellPress
OPEN ACCESS

Article

The intrinsically disordered region of coronins fine-tunes oligomerization and actin polymerization

Xiao Han,[1,3] Zixin Hu,[1,3] Wahyu Surya,[1] Qianqian Ma,[1] Feng Zhou,[1] Lars Nordenskiöld,[1] Jaume Torres,[1] Lanyuan Lu,[1] and Yansong Miao[1,2,4,*]

[1]School of Biological Sciences, Nanyang Technological University, Singapore 637551, Singapore
[2]Institute for Digital Molecular Analytics and Science, Nanyang Technological University, Singapore 636921, Singapore
[3]These authors contributed equally
[4]Lead contact
*Correspondence: yansongm@ntu.edu.sg
https://doi.org/10.1016/j.celrep.2023.112594

SUMMARY

Coronins play critical roles in actin network formation. The diverse functions of coronins are regulated by the structured N-terminal β propeller and the C-terminal coiled coil (CC). However, less is known about a middle "unique region" (UR), which is an intrinsically disordered region (IDR). The UR/IDR is an evolutionarily conserved signature in the coronin family. By integrating biochemical and cell biology experiments, coarse-grained simulations, and protein engineering, we find that the IDR optimizes the biochemical activities of coronins *in vivo* and *in vitro*. The budding yeast coronin IDR plays essential roles in regulating Crn1 activity by fine-tuning CC oligomerization and maintaining Crn1 as a tetramer. The IDR-guided optimization of Crn1 oligomerization is critical for F-actin cross-linking and regulation of Arp2/3-mediated actin polymerization. The final oligomerization status and homogeneity of Crn1 are contributed by three examined factors: helix packing, the energy landscape of the CC, and the length and molecular grammar of the IDR.

INTRODUCTION

Coronins were first identified in *Dictyostelium*, in which they localize on "crown-shaped" F-actin structures at the dorsal cell surface.[1] Subsequently, coronins were found to be highly conserved eukaryotic actin-binding proteins (ABPs) spanning from yeast to human that regulate actin cytoskeleton polymerization and remodeling.[2–6] A lack of coronins results in defects in various cellular processes, such as cell motility,[7–15] cytokinesis,[13,15] endocytosis,[13,16–19] immune cell function,[20–24] and actin turnover.[7,13,25,26] The inter- and intramolecular interactions of coronin proteins with F-actin and other ABPs are critical to regulate coronin function at different steps of actin polymerization, including inhibition of actin nucleation through interaction with the Arp2/3 complex,[7–10,21,22,27–29] actin bundling through direct association with F-actin,[1,10,30,31] and actin depolymerization in cooperation with ADF/cofilin.[25,26,32–35]

In early studies, coronins were subdivided into short and long coronins based on the domain composition.[2,5] Short coronins have a general three-domain composition, including a family-conserved β-propeller domain at the N terminus for actin binding and intracellular localization,[10,22,27,30,31,36–42] an oligomeric coiled-coil (CC) domain at the C terminus,[42–50] and a middle "unique region" (UR) that is variable in sequence and length, while long coronins contain two tandem-arrayed β-propeller domains and lack a CC region. CC-mediated oligomerization is functionally related to diverse coronin activities, including *in vivo* localization, coronin-mediated actin bundling, and Arp2/3 complex inhibition, through the multimerization of the β-propeller domain.[7–10,21,30,42,43,49] The oligomerization state of coronins has been examined in several species using different methods; they exist as dimers,[31,44,48] trimers,[43,47,49] tetramers,[46,50] or oligomers.[10,42] However, how different oligomerization statuses are precisely regulated to provide functions for specific cellular needs remains unclear.

In budding yeast, both the β-propeller (aa 1–400) and the CC (aa 600–651) domains of Crn1 are indispensable for maintaining its localization on cortical endocytic actin patches[3,27,51] and regulating Arp2/3 complex activities[27,29,49] and cofilin-mediated depolymerization.[32,35] However, we have limited knowledge of the Crn1 UR (401–604 aa) as well as the known microtubule-binding[30] and Arp2/3 complex interaction.[49] Here, we identify a function of the UR in optimizing the oligomerization of the Crn1 CC and, thereby, Crn1's functions. The Crn1 UR is a highly flexible intrinsically disordered region (IDR), a hallmark of all short coronins. First, the IDR provides structural flexibility for the neighboring β propeller and CC in maintaining the proper conformation and function of Crn1. Second, the IDR maintains an optimized tetrameric Crn1 by regulating the oligomerization of the CC. *De novo* oligomer engineering further validated that Crn1 tetramerization is the optimum state both *in vitro* and *in vivo* for actin patch localization and biochemical activities in F-actin bundling and Arp2/3 complex inhibition. Strikingly, the IDR length in coronin family proteins has an intriguing evolutionary

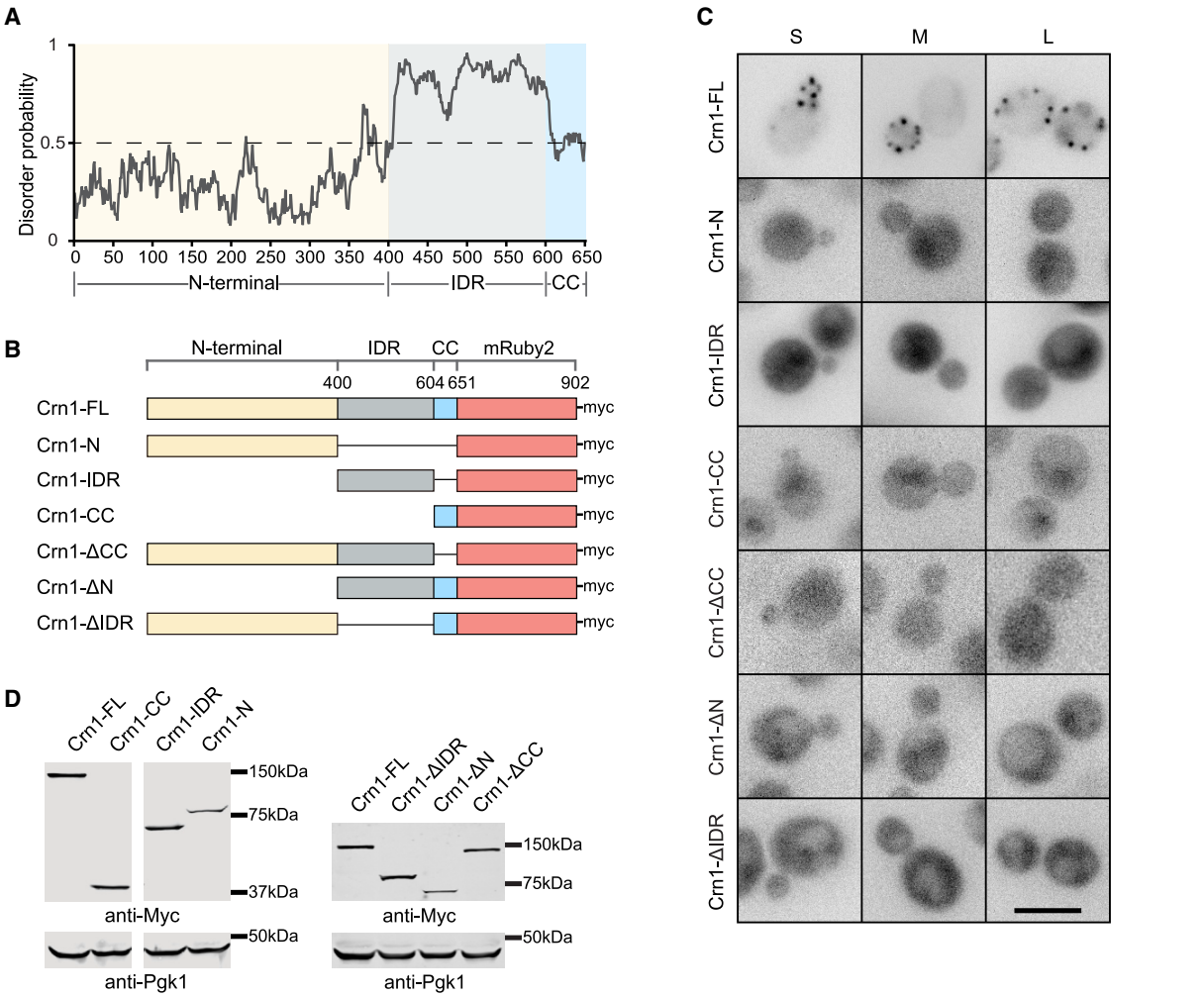

Figure 1. IDR is indispensable for Crn1 localization at actin patches

(A) IDR prediction using IUPs (website: https://iupred2a.elte.hu/) for Crn1, with a disorder probability of 0.5 as the cutoff.

(B) Schematic representation of yeast *in vivo* expression of full-length (FL) Crn1 and truncated Crn1 variants tagged with mRuby2 and 4×Myc tags at the C terminus under the Crn1 native promoter.

(C) Representative images of mRuby2-tagged Crn1-FL and truncated Crn1 variants *in vivo*. S, small-budded cell; M, middle-budded cell; L, large-budded cell. Scale bar, 5 μm.

(D) Western blot analysis of yeast Crn1 expression in (C) using antibodies against the Myc tag. Anti-Pgk1 was used as a loading control.

pattern; IDRs are generally long in fungi and short in mammals. Through protein engineering, biochemistry, and modeling, we reveal that, depending on the CC domain packing and heterogeneity, the IDR modulates the energy landscape of the CC oligomerization status and fine-tunes oligomeric homogeneity in an IDR length- and sequence-grammar-dependent manner.

RESULTS

IDR is indispensable for Crn1 localization at actin patches and its interaction with actin filaments

To delineate the cooperative functions of all three Crn1 domains, we first analyzed the Crn1 sequence using IUPred2[52,53] and defined Crn1-IDR (aa 401–604) as having an average disorder score of greater than 0.5 (Figure 1A). In addition, the N-terminal β-propeller domain (Crn1-N, aa 1–400) and C-terminal CC domain (Crn1-CC, aa 605–651) were verified based on sequence conservation and CC prediction by DeepCoil2.[54] We then generated genome-integrating plasmids to express truncated variants of Crn1 C-terminally tagged with a monomeric red fluorescent protein (mRuby2) in Δ*crn1* under the control of the endogenous Crn1 promoter (Figure 1B). Full-length Crn1 (Crn1-FL) localized to cortical actin patches, but all six truncated Crn1 variants that lacked one or two domains displayed a diffuse pattern without clear punctate actin patch signals (Figure 1C). The loss of actin patch localization in Crn1 variants without the N or CC region (Figure 1C) is consistent with their previously reported individual and synergistic functions in F-actin binding.[27,30,32,36,55] However, the complete loss of the patch pattern of Crn1-ΔIDR was rather unexpected. To examine whether the mislocalization

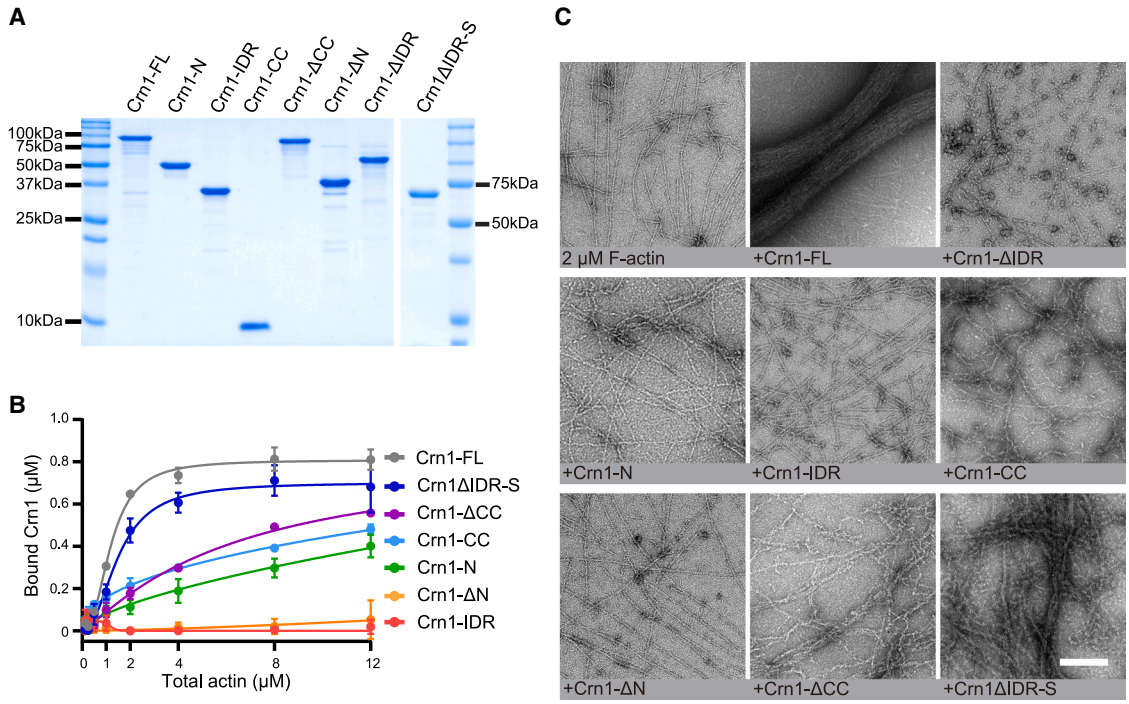

Figure 2. IDR is a flexible linker for the Crn1 conformation and actin binding ability

(A) Coomassie dye-stained SDS-PAGE gel of purified recombinant Crn1 protein variants.

(B) The binding isotherm for Crn1-FL and truncated Crn1 variants in F buffer was determined using high-speed actin cosedimentation assays. A fixed concentration of 1 μM Crn1 protein was mixed with a range of F-actin concentrations from 0 to 12 μM. The mixture was centrifuged at 100,000 × *g* for 30 min at 24°C, and Crn1 in the pellet was analyzed by SDS-PAGE. The amount of coronin in the pellet (μM) was measured and plotted against the F-actin concentration (μM). The Hill equation was used to fit and quantify the results from three technical replicates; data points are presented as the mean ± SD. See also Figure S2A.

(C) Representative negatively stained transmission electron microscopy (TEM) images of preassembled F-actin (2 μM) incubated with Crn1 variants at 1 μM in F buffer. Scale bar, 200 nm.

of Crn1-ΔIDR was due to a change in protein expression or degradation, we characterized the expression of truncated Crn1 variants *in vivo*, and Crn1-ΔIDR showed a protein expression level similar to that of Crn1-FL (Figure 1D).

To understand the mechanism underlying such IDR-dependent localization, we then obtained the recombinant Crn1-FL protein and the same set of truncated variants (Figure 2A). From size-exclusion chromatography (SEC), we found that Crn1-ΔIDR displayed a closer peak-to-void volume than Crn1-FL (Figure S1A), indicating the formation of high-order assemblies, which were observed by transmission electron microscopy (TEM) (Figure S1B). Such behavior of Crn1-ΔIDR suggests that IDR possibly maintains the appropriate Crn1 conformation and folding between the bulk N terminus and the oligomerized C terminus. To validate this hypothesis, we additionally purified a Crn1 variant that randomly retained a 40-aa short fragment of native IDR (Crn1ΔIDR-S; Figures 2A and S1C) and used high-speed ultracentrifugation to quantitively measure the solubility of these Crn1 proteins. Consistent with the aggregation behavior, approximately half of the Crn1-ΔIDR was found in the pellet fraction (Figures S1D and S1E). Crn1-FL and Crn1-ΔIDR-S and other truncated Crn1 variants mainly remained in the supernatant (Figures S1D and S1E). This finding indicates that IDR acts as a flexible linker spacing adjacent domains to prevent misfolding and abnormal protein assembly. We next examined F-actin binding via a high-speed actin cosedimentation assay to measure the interactions of purified Crn1 variants with F-actin. We subjected a fixed concentration of Crn1 variant with a range of concentrations of F-actin. We observed that Crn1-FL exhibited the strongest binding to F-actin, with maximal pelleting occurring at 4 μM F-actin (Figures 2B and S2A). This finding is consistent with previous reports of high affinity binding between Crn1-FL and actin.[30] F-actin binding was also observed for Crn1-N, a known F-actin binding domain,[36] as well as Crn1-ΔCC, which contains the N terminus and IDR (Figures 2B and S2A). Crn1-ΔN showed negligible actin binding activity due to the absence of Crn1-N (Figures 2B and S2A). Moreover, we found that Crn1-CC can bind to F-actin, but with significantly lower affinity compared with the full-length protein (Figures 2B and S2A).[32] Interestingly, Crn1-IDR did not show apparent affinity toward F-actin (Figures 2B and S2A), which suggests that the absence of Crn1-ΔIDR colocalization with actin patches (Figure 1C) was not due to the loss of a direct interaction between the IDR and F-actin. Crn1ΔIDR-S, the soluble IDR truncation variant, displayed mild defects in actin binding compared with Crn1-FL (K_d is ~1.5 μM compared with ~1.24 μM for Crn1-FL; Figures 2B and S2A). The low solubility of Crn1-ΔIDR hampered its use in high-speed actin cosedimentation to characterize F-actin binding. Therefore, we directly compared F-actin bundling by different Crn1 variants under an electron

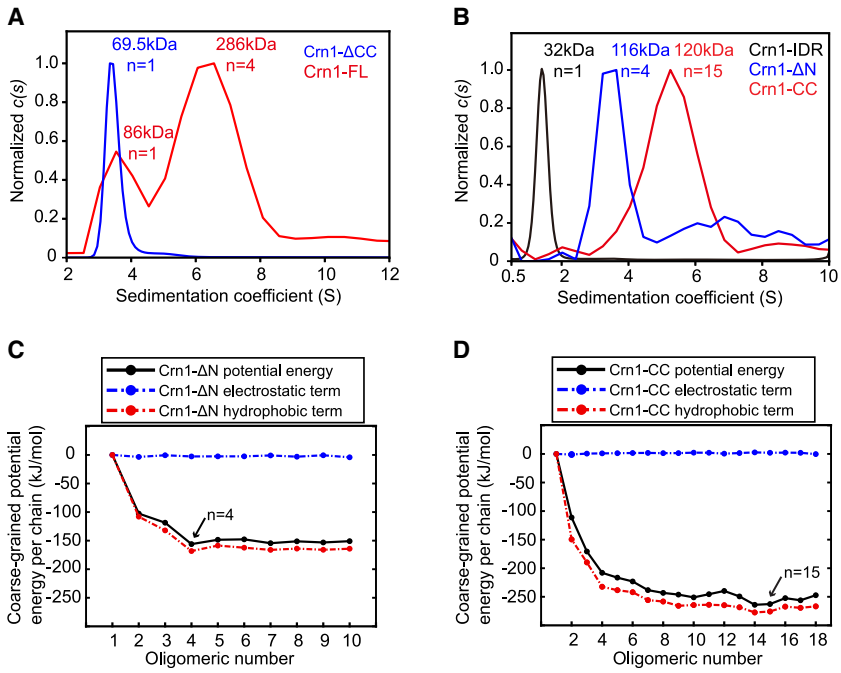

Figure 3. IDR regulates Crn1-CC oligomerization

(A and B) Overlaid AUC-SV profiles of Crn1 protein variants. Sedimentation coefficient distribution *c*(*s*) profiles of Crn1-FL (8.5 μM) and Crn1-ΔCC (9.2 μM) (A) and Crn1-ΔN (4.25 μM), Crn1-IDR (3 μM), and Crn1-CC (3 μM) (B) are shown. The *c*(*s*) distribution was normalized to max *c*(*s*) in GUSSI. Estimated molecular weights and oligomeric states are indicated.

(C and D) Potential energy per chain of Crn1-ΔN (C) and Crn1-CC (D) varies with the number of helices in coarse-grained simulations. Potential energy was decomposed into a hydrophobic term and an electrostatic term for analysis of their contributions.

microscope. Neither the single domains alone (Crn1-N, Crn1-IDR, or Crn1-CC) nor the domain-truncated variants (Crn1-ΔN, Crn1-ΔIDR, Crn1ΔIDR-S, or Crn1-ΔCC) were able to bundle F-actin similar to Crn1-FL (Figure 2C). Importantly, in the presence of F-actin, Crn1-ΔIDR showed heterogeneous ring-like assemblies without an obvious association with actin filaments (Figure 2C), suggesting the indispensable role of the IDR in maintaining the appropriate Crn1 conformation and folding to prevent dysfunctional self-assemblies. Notably, the decreased F-actin bundling by Crn1ΔIDR-S suggests the roles of the IDR in Crn1-mediated F-actin cross-linking.

IDR regulates Crn1-CC oligomerization

CC-mediated oligomerization is critical for Crn1 function. The defects in F-actin cross-linking by Crn1ΔIDR-S motivated us to test whether IDR could modulate the oligomerization of neighboring CCs. We first characterized the structural properties of recombinant Crn1-CC and Crn1-IDR using circular dichroism spectroscopy,[56–58] which showed their distinctive features in indicating disorder (Figure S2B) and a helical conformation (Figure S2C). The murine coronin 1A CC was characterized as a trimer by X-ray crystallography in *in vitro* and *in vivo* assays (Figure S2D).[43,47] A seven-residue motif (abcdefg) called a "heptad" is used to visualize the helical pattern of the coiled coil (Figure S2D),[59–61] in which the "a" and "d" positions are hydrophobic residues.[61–66] DeepCoil2 analysis[54] shows that most heptads of Crn1-CC are occupied by Leu and Val at the "a" and "d" positions (Figure S2E), but not the middle heptad (circled residues; Figure S2E). Such heterogeneity in heptads prevents an accurate prediction of the precise oligomeric state of the CC, either empirically or by relying on CC prediction algorithms.[67]

To quantitatively determine the oligomerization state of Crn1-FL and its truncated variants, we next performed analytical ultracentrifugation sedimentation velocity (AUC-SV) experiments under physiological ionic strength with 150 mM NaCl. Crn1-FL (red curve; Figure 3A) sedimented as two species with sedimentation coefficients of 3.6S (MW_{app} 86 kDa) and 6.5S (MW_{app} 286 kDa), consistent with monomers and tetramers, respectively. Deletion of the C-terminal CC domain (Crn1-ΔCC) produced a single band at 3.4S (MW_{app} 69.5 kDa), corresponding to a monomeric form (blue curve; Figure 3A). Thus, the tetrameric form of Crn1 requires the CC domain. Next, we asked if the CC domain is sufficient for Crn1 tetramerization. To our surprise, the *c*(*s*) profile of Crn1-CC showed a single peak at 5.3S (MW_{app} ~120 kDa), close to the peak predicted for a pentadecamer (red curve; Figure 3B). In contrast, Crn1-ΔN, which contains both the CC and the IDR domains, showed a single species at 3.4S with an MW_{app} of ~116 kDa, consistent with a tetramer (blue curve; Figure 3B). Such results suggest that, although the IDR domain alone is a monomer (black curve; Figure 3B), it is critical in maintaining the tetrameric state of the adjacent CC domain, which otherwise forms higher-order oligomers.

The IDR has been reported to modulate its own hydration-free energy and that of the connected folded domain, which might tune the hydrophilicity of the protein as well as the macromolecular activity.[68] We next asked if the IDR could adjust the energy landscape of the neighboring CC domain. We used coarse-grained molecular simulations to investigate the relationship between the potential energy per chain and the degree of oligomerization. We simultaneously simulated Crn1-ΔN and Crn1-CC, the CC domain with and without the IDR, respectively. Since knowledge about the arrangement of chains in Crn1-CC oligomers was limited, starting configurations arranged in both parallel and antiparallel alignments were tested, and coarse-grained simulations actually showed indistinguishable results for the two kinds of alignments (Figure S2F). Thereafter, we used only the parallel orientation in subsequent simulations. Consistent with the AUC-SV experiments (Figure 3B), the coarse-grained potential energy per chain did not drop further after the tetrameric state was reached for Crn1-ΔN, showing a maximum

stabilization effect at the tetrameric state (black curve; Figure 3C). Decomposition further showed that hydrophobic interactions contribute a dominant effect in guiding the overall potential energy per chain along with the examined oligomerization states of Crn1-ΔN (red curve; Figure 3C). In contrast, electrostatic interactions had a negligible effect on the optimization of Crn1-ΔN oligomerization (blue curve; Figure 3C). Surprisingly, without the IDR, the potential energy per chain of Crn1-CC showed a further decrease after the tetrameric state was reached, until the tetradecameric-to-pentadecameric state transition, suggesting that Crn1-CC alone tends to form high-order oligomers in the absence of the IDR (Figure 3D), again consistent with the AUC-SV results (Figure 3B). Similar to Crn1-ΔN, hydrophobic interactions, rather than electrostatic interactions, within Crn1-CC were the underlying regulatory factors that determined the optimal oligomeric number, additionally supporting the critical roles of hydrophobic interactions between heptad repeats of Crn1-CC.[61–66]

Optimized oligomerization of Crn1 regulates Crn1 functionality *in vivo*

Coronin *in vivo* homooligomers have been investigated by density gradient centrifugation and gel-filtration chromatography.[43,45,50] However, it is challenging to quantify the *in vivo* oligomer states for the proteins that are able to undergo tunable heterogeneous self-assembly, oscillating between different oligomeric orders and often cosedimenting with associated binding partners. In addition, the oligomeric status for tunable oligomers is sensitive to the conditions used for cell lysate preparation. Here, we expressed and purified Crn1 from yeast cells (namely, yCrn1-FL)[69] (dashed box; Figure 4A) subjected to AUC analysis (Figure 4A). yCrn1-FL displayed heterogeneity, where 2D size-and-shape analysis showed two major populations, including tetrameric states (P1 and P3, 55%; Figure 4A) and a hexamer form (P2, 35%; Figure 4A). Based on the fictional ratio f/f_0 that is related to the particle shape, the tetrameric yCrn1-FL proteins were mixed with elongated (P1, $f/f_0 > 2$) and globular species (P3, $f/f_0 \sim 1.2$) (Figure 4A), whereas bacterial purified tetrameric Crn1-FL proteins were mainly elongated ($f/f_0 > 2$) (Figure S2G).

To dissect the complex heterooligomers, we employed a protein engineering approach to determine the oligomerization-status-dependent functions of yeast Crn1 both *in vivo* and *in vitro*. Here, we designed and engineered Crn1 variants at different homooligomeric states, ranging from dimer to pentamer, by replacing the Crn1 CC domain with several well-characterized homooligomeric CC motifs[70–73] (Figure 4B). *De novo*-designed *CRN1* variants underwent genomic integration into the background of *crn1*Δ yeast under the endogenous promoter and were tagged by C-terminal mRuby2, allowing *in vivo* examination of their localization at actin patches. All the engineered homooligomeric Crn1 variants were expressed at similar protein levels *in vivo* (Figure 4C). Homooligomeric Crn1 variants generally maintained actin patch localization (Figure 4D), indicating an association with F-actin even with different oligomerization statuses.[30,51] By quantifying the signal ratios of Crn1 variants on the actin patch over the total cellular signals (Figure S3A), we found that Crn1ΔCC-Di and Crn1ΔCC-Tri at lower oligomeric states exhibited lower signal enrichment on actin patches than higher-level oligomeric Crn1 variants, Crn1ΔCC-Tet, and Crn1ΔCC-Pent, as well as Crn1 WT (Figure 4E). The last three variants showed similar actin patch signal ratios, suggesting a similar functional association with F-actin in the patch.

To evaluate the *in vivo* fine-tuning of Crn1 functionality by different homooligomeric variants, we introduced them into *arc35-5*,[74]which exhibits a negative genetic interaction with *crn1*Δ.[27,28] At a semipermissive temperature of 34°C (Figure S3B), *crn1*Δ *arc35-5* exhibits severe synthetic sickness, which is similar to a lack of any individual domain among the IDR, the CC, or the N-terminal β propeller in *arc35-5* (Figure S3B). Interestingly, while *arc35-5 crn1ΔCC-Di* and *arc35-5 crn1ΔCC-Tri* showed similar growth defects compared with *crn1*Δ *arc35-5* at 34°C, *arc35-5 crn1ΔCC-Tet* and *arc35-5 crn1ΔCC-Pent* exhibited obviously higher viability (Figure 4F). Both actin patch localization and growth assays demonstrated a better functionality of tetrameric and pentameric Crn1 than the dimeric or trimeric variants, suggesting the necessity of maintaining Crn1 oligomerization for optimal functionality.

Crn1 oligomeric state regulates F-actin cross-linking and inhibition in Arp2/3-mediated actin nucleation *in vitro*

To further quantitatively characterize the biochemical functions of engineered homooligomeric Crn1 variants, we first purified the Crn1 homooligomeric variants using an *E. coli* expression system (Figure 5A) and examined their oligomerization state by AUC-SV. All Crn1 variants displayed the expected oligomeric form, with one band in the *c*(*s*) plots (Figure 5B). Next, we compared their actin-bundling activities via a low-speed actin cosedimentation assay under physiological ionic strength with 150 mM KCl. Interestingly, we found that the Crn1 variants cross=linked F-actin in an oligomerization state-dependent manner. Crn1ΔCC-Tet and Crn1ΔCC-Pent, which are high-level oligomers, demonstrated higher bundling efficacy than Crn1-ΔCC-Di and Crn1ΔCC-Tri (Figures 5C and S3C). We also directly visualized the bundling of F-actin using total internal reflection microscopy (TIRF) in the presence of different homooligomeric Crn1 variants and quantified the bundling efficacy by measuring "skewness."[75,76] Similar oligomerization-dependent actin cross-linking was observed (Figures 5D and 5E). These results suggest that F-actin bundling ability is positively correlated with the valency of the Crn1 N terminus.

Yeast and mammalian coronins have been shown to inhibit the Arp2/3 complex in actin nucleation and branching in a CC-dependent manner.[7,8,10,21,22,27,49] We next compared the inhibition of the Arp2/3 complex by Crn1ΔCC-Di and Crn1ΔCC-Tet, representing the lower- and higher-level oligomeric states, respectively. We quantitatively examined nucleation promoting factor (NPF)-Arp2/3-mediated actin nucleation and branching over time (Figures 5F and 5G and Video S1) using the polyproline plus VCA (polypVCA) domain of Las17/WASp[77] (Figure S3D). Wild-type (WT) Crn1 (Crn1-FL) showed apparent inhibition of both actin nucleation and branching on the Arp2/3 complex, resulting in decreased overall actin polymerization (Figures 5F and 5G and Video S1), consistent with previous work.[7,8,22,27]

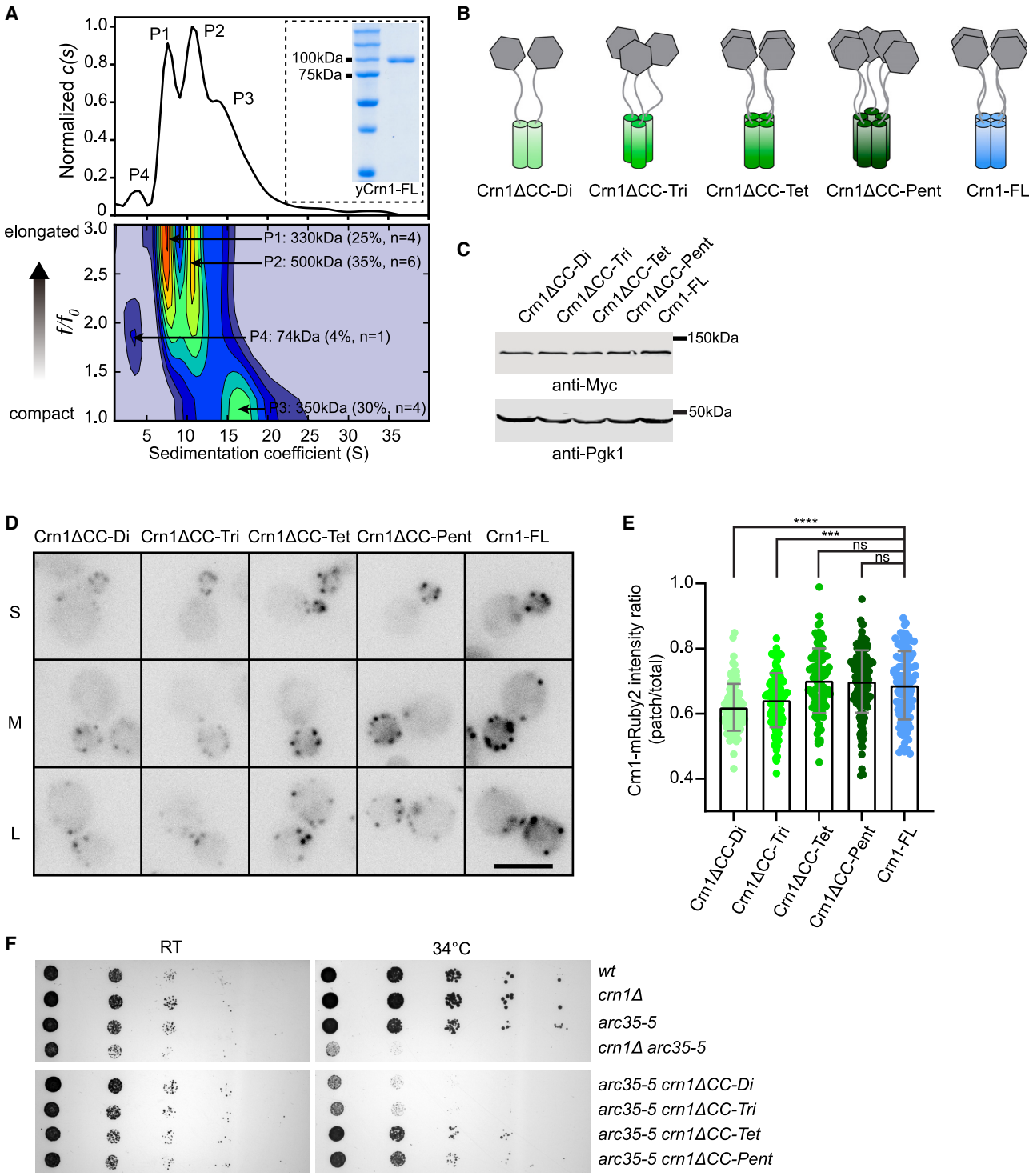

Figure 4. Optimized oligomerization of Crn1 regulates Crn1 functionality *in vivo*

(A) Size and shape distribution profile of yeast purified full-length Crn1 (namely, yCrn1-FL) (5.8 μM) as shown in the dashed box from AUC-SV experiments performed in 50 mM Tris (pH 8.0) and 150 mM NaCl buffer and analyzed by the *c*(*s*, *ff0*) model. Different populations (P1 to P4) shown in the *c*(*s*) profile were analyzed by the sedimentation coefficient (S) and frictional ratio (*f*/*f0*), and a heatmap was generated (bottom). The color in the heatmap indicates the concentration of different populations, from lowest (blue) to highest (red). An increasing value of *f*/*f0* indicates elongated or nonglobular species. The size and percentage (by peak area) of each population are indicated.

(legend continued on next page)

However, deletion of the CC domain (Crn1-ΔCC) did not inhibit the Arp2/3 complex, highlighting the importance of Crn1 oligomerization in inhibiting the NPF-Arp2/3 complex (Figures 5F and 5G and Video S1). These results are consistent with findings from previous pyrene-actin assays on Crn1.[27] Under the same experimental conditions, dimeric (Crn1ΔCC-Di) and tetrameric (Crn1ΔCC-Tet) Crn1 variants impaired polypVCA-Arp2/3 complex-mediated actin polymerization to different degrees. Crn1-ΔCC-Tet behaved like Crn1-FL, effectively inhibiting Arp2/3-polypVCA complex-mediated actin branching (Figures 5F and 5G and Video S1). In contrast, Crn1ΔCC-Di exerted a much lower inhibitory effect. Compared with Crn1-ΔCC, however, Crn1ΔCC-Di still had a slight negative impact on Arp2/3-NPF activities (Figures 5F and 5G and Video S1). These findings indicated that Crn1ΔCC-Di was still partly functional, consistent with its partial defect in actin patch localization and partial rescue of the genetic sickness of the *crn1*Δ *arc35-5* double mutant (Figures 4E and 4F). In addition, we examined the oligomerization of Crn1ΔIDR-S (Figure S3E). Unlike Crn1-FL, Crn1-ΔIDR-S was present as a mixture of trimers and hexamers with sedimentation coefficients of 8.2S and 13S, corresponding to sizes of 166 and 322 kDa, respectively. An f/f_0 close to 1.2 indicates a compact conformation with a shortened IDR linker. Crn1ΔIDR-S showed decreased localization on actin patches (Figures S4A–S4C), no apparent rescue of the genetic sickness of *crn1*Δ *arc35-5* (Figure S4D), compromised F-actin bundling (Figure S4E), and a weaker inhibitory effect than Crn1-FL on the Arp2/3 complex (Figure 4F and Video S2). Taken together, the aforementioned *in vivo* and *in vitro* functional characterization suggests that Crn1 function depends on its oligomeric state. Among the range of oligomerization states we examined here, tetrameric Crn1 demonstrated better functionality than lower-level Crn1 oligomers.

Evolutionary conservation of IDRs in coronin family proteins

The function of the IDR in fine-tuning CC domain oligomerization motivated us to ask whether and how this mechanism is evolutionarily conserved. We analyzed the IDR at the N terminus of the CC domain across coronin family proteins. We collected 392 coronin homologs from 200 species, including species from all major phyla, based on a previously reported phylogenetic analysis of coronin proteins,[78] and generated a taxonomic tree from these homologs (Figure 6). We defined their IDRs by their position between the β propeller and the CC domain, as well as by low-complexity analysis by IUPs (website: https://iupred2a.elte.hu/). We found that the presence of the IDR is evolutionarily conserved among coronin family proteins, although the IDR is conserved in neither sequence nor length, which is a common feature of the IDR.[79,80] Coronins in only 3 of 200 species, *T. vaginalis* (protozoan), *A. anophagefferens* (protozoan), and *B. natans* (unicellular eukaryotic alga), do not contain an IDR. Then, we manually mapped the analyzed IDR into the coronin taxonomic tree (named IDR-MAP hereafter), in which the IDR length is shown in scale (Figure 6). Strikingly, we found that, although the IDRs vary in general, they follow a clustered pattern in which the IDR lengths within each taxonomic clade are similar but clearly different from those of other clades. The coronins of most protozoa (including SAR, Excavata, and Amoebozoa) contain a short IDR (<50 aa), and coronins from only Trypanosomatidae of Excavata and Aconoidasida of Alveolata contain a long IDR (between 50 and 100 or >100 aa). However, in the fungal kingdom, all coronins under Ascomycota (branch marked with a black star), including *S. cerevisiae*, carry a long IDR (>150 aa). In contrast, coronins in most metazoans, especially mammals, have a short IDR (<90 aa), except for Nematoda, in which the IDR is generally longer (>150 aa). Our coronin IDR-MAP suggests a potential evolutionary selection mechanism that determines IDR length.

The IDR of human coronin 1A is essential for its *in vivo* functionality but independent of IDR functions in turning CC oligomerization

The evolutionarily conserved presence of the IDR in coronin proteins (197 of 200 species) prompted us to ask why the IDR is universally present but varies in length among homologs. We investigated the human coronin homolog Coronin 1A as a representative highly eukaryotic coronin homolog.[2,24,43] We first visualized the *in vivo* localization of full-length Coronin 1A (Coro1A-FL) and its IDR-truncated variant (Coro1A-ΔIDR) (Figure S4G) by overexpressing C-terminal-tagged GFP fusion proteins in transiently transfected mouse embryonic fibroblasts (MEFs). Fluorescence patterns of Coronin 1A fusions in living cells were imaged by spinning-disk confocal microscopy and analyzed. GFP-fused full-length Coronin 1A formed bright puncta around the cell cortex and filamentous structures (Coro1A-FL; Figure 7A). However, GFP-fused Coro1A-ΔIDR became diffusible in the cytosol and abolished its specific localization, similar to the GFP pattern in the vector control (Figure 7A). Quantification of cortical enrichment of Coro1A-FL clearly distinguished its pattern from Coro1A-ΔIDR (Figures 7B and S4H), suggesting the necessity of the IDR in maintaining the human coronin *in vivo* localization, similar to the IDR for yeast Crn1.

(B) Cartoon diagram of *de novo*-designed homooligomeric Crn1 variants. *In vivo* yeast expression was achieved through genomic integration with mRuby2 and 4×Myc tags at the C terminus under the native promoter.

(C) *In vivo* homooligomeric Crn1 variants in (B) examined by western blot using total cell lysate and antibodies against Myc-tag. The anti-Pgk1 antibody was used as a loading control.

(D) Representative fluorescence images of mRuby2-tagged homooligomeric Crn1 variants in yeasts. S, small-budded cell; M, middle-budded cell; L, large-budded cell. Scale bar, 5 μm.

(E) Crn1-mRuby2 signal intensity ratio on actin patches (patch/total, see STAR Methods) in (C). From left to right, n = 98, n = 108, n = 95, n = 149, and n = 102 patches. Bar graphs indicate mean values. Error bars: SD.

(F) Yeast spot assay of homooligomeric Crn1 variants in the genetic background of *crn1*Δ *arc35-5*. Cells were grown on YPD at the indicated temperature for 42 h before imaging. Unpaired two-tailed Student's t test assuming equal variance was used to determine differences between two groups in (E), *p < 0.05, **p < 0.01, ***p < 0.001, ****p < 0.0001; ns, not significant.

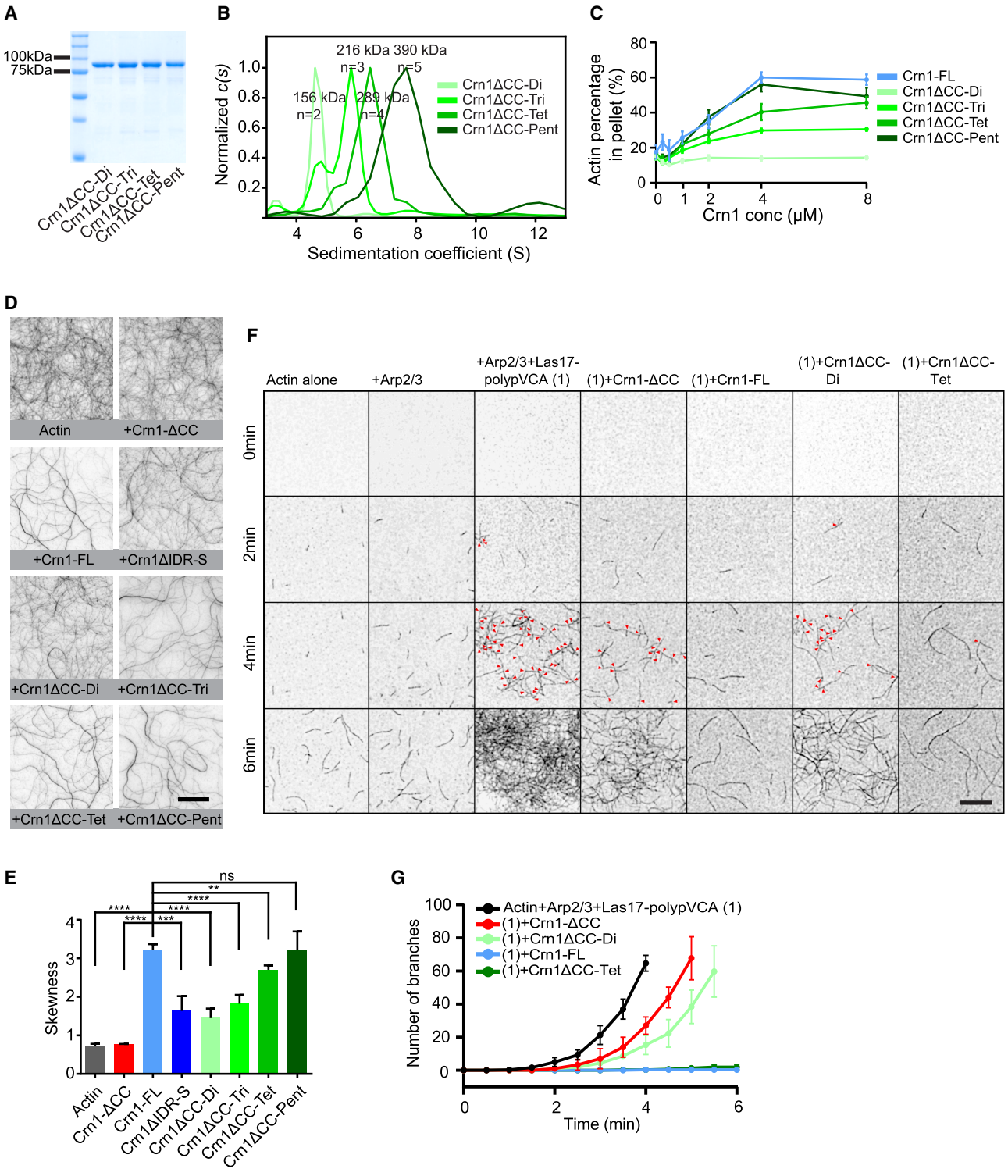

Figure 5. The Crn1 oligomeric state regulates F-actin cross-linking and inhibition in Arp2/3-mediated actin nucleation *in vitro*

(A) Coomassie dye-stained SDS-PAGE gel of purified recombinant Crn1 homooligomer variants in a design similar to that in Figure 4B without C-terminal tags. (B) Overlaid sedimentation coefficient distribution profiles of purified homooligomer Crn1 variants Crn1ΔCC-Di (7.6 μM), Crn1ΔCC-Tri (8.9 μM), Crn1ΔCC-Tet (8.7 μM), and Crn1ΔCC-Pent (9 μM), from AUC-SV experiments performed in 50 mM Tris (pH 8), 150 mM NaCl. The *c*(*s*) distribution was normalized to max *c*(*s*) in GUSSI; estimated molecular weights and oligomeric states are indicated.

(legend continued on next page)

Given that the Crn1 IDR regulates Crn1 CC oligomerization, we next examined whether the IDR of human Coronin 1A possesses the same regulation. Murine Coronin 1A is a parallel homotrimer both *in vivo* and *in vitro*,[43,47] while CC oligomerization of human Coronin 1A is unknown, although the CC sequences of human and murine Coronin 1A are highly similar. We characterized the oligomerization of human Coronin 1A by AUC on synthesized CC (Coro1A-CC) and CC plus IDR (Coro1A-ΔN) peptides (Figure 7C). Both human Coro1A-CC and Coro1A-ΔN proteins sedimented mainly as trimers in AUC-SV experiments (Figure 7C), suggesting an IDR-independent oligomerization of human Coronin 1A.

The evolutionary interplay between IDR length and the stability of CC oligomers

The above different roles of IDRs on different CCs for their oligomerization status motivated us to ask whether the natural CC or the IDR determines the oligomerization status with their combination. We first investigated whether and how different IDRs could influence the oligomerization of the Coronin 1A CC. Here, we used the murine Coronin 1A CC domain (PDB: 2akf; named MmCC hereafter) because it has been validated as a stable homotrimer in crystals and in solution.[43,47] Through coarse-grained simulations, we compared the energy landscape of MmCC fused with three different IDRs of varying lengths: MmCC plus its native IDR (403–429 aa), the short fragment from Crn1ΔIDR-S (484–523 aa), and the full Crn1 IDR (401–604 aa), which were named MmIDR-MmCC, ScSIDR-MmCC, and ScIDR-MmCC, respectively (Figure 7D). We applied the same computational approach used for Crn1-ΔN (Figure 2C) and Crn1-CC (Figure 2D). Intriguingly, all three different combinations showed no further decrease in energy after the trimeric state was reached, indicating that none of the three IDRs altered the oligomeric state of MmCC (Figure 7E), consistent with its known trimer form.[43,47] Such results suggest that the length of the IDR does not influence the oligomerization of well-packed CC domains, such as the mouse Coronin 1A CC domain (MmCC).

To better evaluate the packing of helices and stability of the CC, we assessed how different interactions between the helical chains of MmCC and Crn1-CC were, using the structures from simulated tetrameric Crn1-CC and the crystal of MmCC. Previous studies have reported that interactions between heptad position pairs "a"-"a" and "d"-"d" constitute a hydrophobic core, while "e"-"g" often forms a salt bridge.[62,63,65] We used the motif-averaged contact map to describe the interaction strength between two adjacent helices of tetrameric Crn1-CC and trimeric MmCC (Figure S5A). Between the MmCC helices, the heptad position pairs in which strong interactions occurred were "a"-"a", "a"-"d", "d"-"d", and "e"-"d", matching the pattern of the hydrophobic core (MmCC; Figure S5B). However, Crn1-CC displayed a varying interaction pattern, including many other heptad-position pairs with low contact probability, suggesting relatively unstable helical packing compared with that of MmCC (Crn1-CC; Figure S5C). The difference between two motif-averaged contact maps of two coronin homologs was further demonstrated by the motif-contact difference map (Figure S5D). Interestingly, when different IDRs were linked to MmCC, the pattern and strength of the interactions between MmCC helices were not substantially altered by any of the three tested types of IDRs (Figures 7F and S5E). For example, the motif-averaged contact map of MmCC with full Crn1 IDR (ScIDR-MmCC) was only slightly changed compared with that of MmCC alone (Figures 7F and S5B). This difference was expressed as the Euclidean distance, which was 0.17 between ScIDR-MmCC and MmCC (Figures 7F and S5B). In contrast, with Crn1-IDR, Crn1-CC showed a much greater change in preexisting interactions, resulting in a Euclidean distance of 0.28 without introducing any heptad position pairs with new interactions (Figures 7G and S5C). The above analysis results demonstrate that the IDR modulates the packing of Crn1-CC helices, which are unstable, possibly due to nonideal interacting residues, but has a less pronounced influence on the well-packed MmCC. Such evolved CC domain sequences and packing patterns of coronin family proteins may thereby contribute to the evolutionary selection of IDR length.

The above analysis of Crn1-CC from coarse-grained simulations suggests the possibility that a long IDR maintains a functional tetrameric state of Crn1 by tuning the unstable packed Crn1-CC. However, our earlier experiments using truncation on the native sequence of Crn1 IDR (Crn1ΔIDR-S) always mixed with two factors of length and sequence specificity. We designed three additional Crn1 constructs that carry identical Gly-Ser repeats but varied lengths of 50 aa (Crn1-DIR-50), 100 aa (Crn1-IDR-100), and 204 aa (Crn1-IDR-204, the same as WT Crn1) (Figure 7H). We purified these three engineered Crn1 variants from *E. coli* (Figure 7H) and performed AUC-SV experiments under physiological ionic strength with 150 mM NaCl. As a result, three Crn1 variants exhibited a mixture of trimer and higher oligomers but with different heterogeneity in a length-dependent manner (Figure 7I). The overlaid *c*(*s*) profiles show a distribution of three populations (peaks 1 to 3; Figures 7I and 7J). Peak 1 is the trimeric population, which is a dominant peak for all compared proteins (Figures 7I and 7J). In contrast, the second major

(C) F-actin bundling profile from a low-speed actin cosedimentation assay using homooligomeric Crn1 variants in buffer with a physiological ionic strength of 150 mM KCl. Actin bundling was measured by quantifying the actin amount in the pellet fraction through densitometry from an SDS-PAGE gel using ImageJ, from three technical replicates; data points are presented as the mean ± SD. See also Figure S3C.

(D) TIRF images showing Crn1-mediated actin bundling by different Crn1 variants after 90 min. Actin (1 μM) was copolymerized with Crn1 variants (2 μM) in buffer with a physiological ionic strength of 150 mM KCl. Scale bar, 10 μm.

(E) Quantification of the bundling level in the region of interest (ROI) (32 × 32 μm^2) from (D) by skewness of pixel intensity. Bar graphs indicate mean values (n = 4 ROIs for each sample; error bars: SD).

(F) Representative time-lapse TIRF images of Arp2/3-mediated actin polymerization in the presence of the indicated Crn1 variants, including 1 μM actin, 5 nM Arp2/3 complex, 25 nM Las17-polypVCA, and 100 nM Crn1 variants. Scale bar, 10 μm. Corresponding Video S1 is available online.

(G) Quantification of actin branch number in the ROI (32 × 32 μm^2) over the first 6 min of TIRF time-lapse imaging in (F) (n = 3 ROIs for each condition, data points are presented as the mean ± SD). Unpaired two-tailed Student's t test assuming equal variances was used to determine differences between two groups in (E), *p < 0.05, **p < 0.01, ***p < 0.001, ****p < 0.0001; ns, not significant.

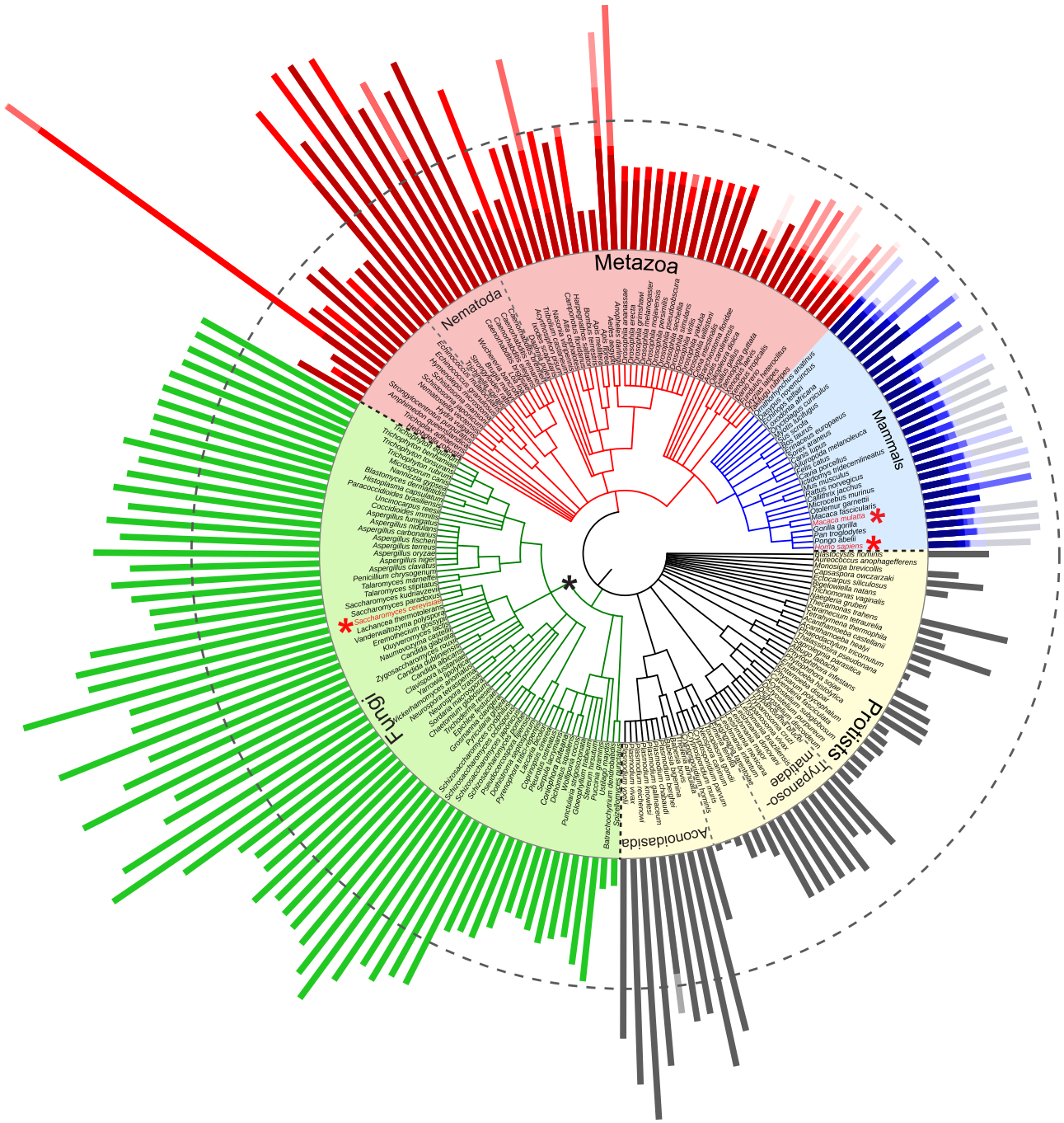

Figure 6. IDR-MAP of coronin family proteins

NCBI common taxonomy tree for 392 coronin homologs from 200 species.[78] The circular tree was rendered using Interactive Tree Of Life (iTOL) (https://itol.embl.de).[81] Three main parts (protists, fungi, and metazoa) are separated by black dashed lines. Bars outside of the tree represent the relative length of coronin IDRs from all analyzed homologs. Additional gradient color bars were overlaid for the species that carry coronin isoforms. The gray dashed circle marks the position with a length of 100 aa. The black asterisk represents blade of Ascomycota. Three red asterisks mark Budding yeast (*S.cerevisiae)*, mouse (*M.mulatta),* and human (*H.sapiens)* in a clockwise order.

population in peak 2 (hexamer or pentamer) and the minor population of peak 3 decrease with increasing IDR length (Figures 7I and 7J), indicating IDR length-dependent regulation in optimizing oligomerization status and thereby homogeneity. However, none of the artificially designed low-complexity sequences form tetramers as native Crn1-FL, including Crn1-IDR-204, with the same length as Crn1-FL. Taken together, our results suggest that the final oligomerization status and homogeneity of the

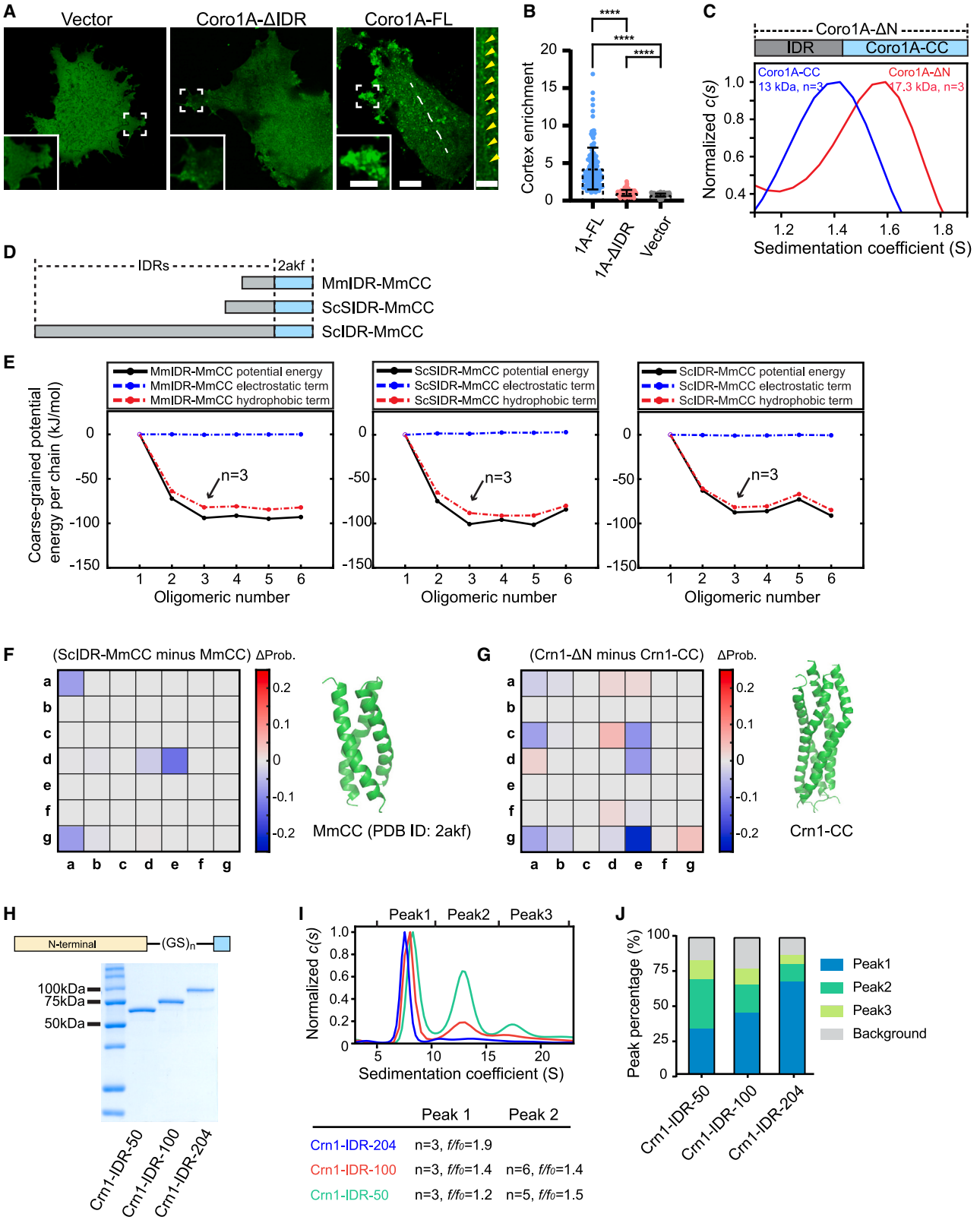

(legend on next page)

coronin CC rely on three factors: heptad-determined helical CC packaging, IDR length, and IDR sequence composition.

DISCUSSION

Oligomerization regulates the biochemical activities of ABPs in actin assembly

The initiation, reorganization, and depolymerization of the actin cytoskeleton are biochemically orchestrated by a diverse array of ABPs, including actin nucleation proteins (e.g., the Arp2/3 complex and formin), G-ABPs (e.g., profilin), an elongation-promoting factor (Ena/VASP), cross-linkers (e.g., fimbrin), and depolymerization factors (e.g., ADF and cofilin).[83–85] Emerging evidence shows that inter- or intramolecular interactions of ABPs and macromolecular assemblies, including lower- to higher-order oligomerization, are fundamental mechanisms in the regulation of their biochemical activities during actin polymerization.[71,75,86–107] For example, during plant immune activation, intermolecular interactions between formin dimers on the plasma membrane enhance formin-mediated actin nucleation.[75,94,100] In mammals, multivalent interactions between WASP and the Arp2/3 complex activate actin nucleation during T cell signal transduction.[101–103] Mammalian Ena and VASP are also known to cluster as tetrameters to enhance actin elongation activity by creating a tetravalent G-actin-binding (GAB) domain through a CC.[71,105,106] F-actin stabilization also requires lower-order ABP oligomerization, such as CC-mediated dimeric interactions between tropomyosins.[89–91] The dimerization of vinculin is also critical for F-actin bundling and engagement of partners at focal adhesion sites.[92,93,104,107] Crn1 oligomerization was reported to regulate Arp2/3 *in vitro*, where a replacement of Crn1 CC by a bacteriophage trimerization domain showed comparable activity in a pyrene-actin polymerization assay.[49] Here, with quantitative TIRF analysis and precise oligomerization protein engineering, we demonstrated oligomerization status-dependent Crn1 activity in inhibiting the Arp2/3 complex, and cross-linking of F-actin (Figures 3, 4, and 5), which is regulated by neighboring IDR. However, simply altering the oligomerization state of Crn1 is not enough to entirely relocate it from actin patches. Even when Crn1 transitions from a dimer to a pentamer, its displacement from patches to the cytoplasm remains moderate (Figures 4D and 4E). The crucial role of IDR in maintaining proper localization is that of being a flexible linker, which connects the N-terminal and C-terminal domains and prevents their conformational clashes. When the IDR is removed (Crn1-ΔIDR), the resulting assembly is prone to aggregation, and proper localization is lost. The interaction between coronin and other proteins may also play a role in preserving its functional localization. In yeast, β-propeller and CC domains have been indicated to maintain Crn1 patch localization through F-actin binding.[30,32,51] IDR has also been reported to interact with the Arp2/3 complex by fluorescence anisotropy competition assay,[49] where Crn1 competes with the Arp2/3 complex in binding with rhodamine-labeled VCA, and an IDR (411—593 aa) truncation version abolishes such competition. In mammalian cells, cortex localization of Coronin 1A in T cells[21–23] and leading-edge localization of Coronin 1B in fibroblasts[7–10] were associated with Arp2/3 complex and F-actin, respectively, through the coronin N terminus. Although IDR-mediated interaction is unknown in mammalian coronin homologs, a partial truncation of the mouse Coronin 1A IDR (400–416 aa) lost cytoskeleton association, whereas its trimeric status remains.[43] Overall, how different intermolecular interactions of coronin homologs orchestrate their F-actin association and localization is worth future investigation.

Figure 7. Oligomerization and homogeneity of the coronin CC rely on multiple factors

(A) Representative live-cell images of MEFs expressing GFP from vector, GFP-fused Coro1A-ΔIDR, and Coro1A-FL. Zoomed images represent the area in the white dashed boxes. For Coro1A-FL, an additional white dashed line and a magnified view (right side) indicate the filament structure (yellow arrowheads) in the cytosol. Scale bars from left to right, 5, 10, and 5 μm.

(B) Quantification of cortex enrichment of GFP-fused Coro1A proteins in MEFs. Vector, n = 114 from 10 cells. Coro1A-ΔIDR, n = 110 from 9 cells. Coro1A-FL, n = 146 from 13 cells. Bar graphs indicate the mean values. Error bars: SD.

(C) Overlaid sedimentation coefficient distribution *c*(*s*) profiles of Coro1A-CC (81 μM) and Crn1-ΔN (54 μM) from AUC-SV experiments performed in 50 mM Tris (pH 8) and 150 mM NaCl. The *c*(*s*) distribution was normalized to max *c*(*s*) in GUSSI. Estimated molecular weights and oligomeric states are indicated.

(D) Cartoon diagrams of murine Coronin 1A CC (PDB: 2akf, named MmCC hereafter) with different IDRs used in the simulations. MmCC plus its native IDR (403–429 aa), a short IDR fragment of Crn1 (484–523 aa), and the full Crn1 IDR (401–604 aa) were named MmIDR-MmCC, ScSIDR-MmCC, and ScIDR-MmCC, respectively.

(E) Potential energy per chain of three combinations of MmCC with the IDRs MmIDR-MmCC (left), ScSIDR-MmCC (middle), and ScIDR-MmCC (right) in coarse-grained simulations. Potential energy was decomposed into a hydrophobic term (red) and an electrostatic term (blue) for analysis of their contributions.

(F) Motif contact difference map between MmCC and ScIDR-MmCC (left) and a representative side view of the MmCC trimer (right). Red and blue in the motif contact difference map indicate an increase and decrease in contact probability, respectively. The representative side view was adapted from its crystal structure (PDB: 2akf).

(G) Motif contact difference map between Crn1-CC and Crn1-ΔN (left) and a representative side view of the Crn1-CC tetramer (right). Red and blue in the motif contact difference map indicate an increase and decrease in contact probability, respectively. The representative side view of Crn1-CC was adapted from the all-atom structure reconstructed from the representative structure in coarse-grained simulations by PULCHRA[82] followed by energy minimization.

(H) Cartoon diagram of Crn1 with artificial IDRs, where native Crn1 IDR was replaced by different lengths of Gly-Ser repeats, named Crn1-IDR-50, Crn1-IDR-100, and Crn1-IDR-204, respectively. Purified proteins are shown by Coomassie blue-stained SDS-PAGE gel (bottom).

(I) Overlaid sedimentation coefficient distribution *c*(*s*) profiles of Crn1-IDR-50 (13 μM), Crn1-IDR-100 (13 μM), and Crn1-IDR-204 (9 μM) from the AUC-SV experiment performed in 50 mM Tris (pH 8) and 150 mM NaCl. The *c*(*s*) distribution was normalized to max *c*(*s*) in GUSSI. The estimated oligomeric states and peak ff_0 values are listed below.

(J) Measurement of the peak percentage for the three coronin proteins in (I). Peak 1 was defined from S 5 to 10, peak 2 was defined from S 10 to 15, and peak 3 was defined from S 15 to 20. Peak percentage was measured by peak area of defined compared with total in GUSSI. Unpaired two-tailed Student's t test assuming equal variances was used to determine differences between two groups in (B), *p < 0.05; **p < 0.01; ***p < 0.001; ****p < 0.0001.

IDR tunes the higher-order assembly and functionality of coronins with evolutionary selection

Short coronins are subdivided into type I (e.g., Coronins 1A, 1B, and 1C) and type II (e.g., Coronin 2A and Coronin 2B) coronins in metazoans and an "unclassified" class in nonmetazoans (e.g., Crn1 of *S. cerevisiae*, coronin of *Dictyostelium*),[78] whereas long coronins are also classified as type III (e.g., POD1) coronins. Our analysis of 392 short coronins from 200 species revealed that IDR is a conserved feature. Previous studies of IDRs of *S. cerevisiae* Crn1 and *D. melanogaster* Dpod1 have shown microtubule-binding abilities.[30,51,108] We revealed a function of IDR that optimizes the tetrameric state of Crn1 by suppressing higher-order CC domain oligomerization. IDR-containing proteins (IDPs) work different from fully structured proteins (e.g., molecular recognition and assembly, protein modification, and spacing chains).[109] IDRs can regulate homo- and heterooligomeric interactions, particularly for dynamic ensembles of macromolecular assemblies.[110,111] Our recent summary of IDPs for endocytosis reported a striking correlation between IDR length and the temporal recruitment of IDPs to actin patches for progressive endocytosis. Earlier endocytic module proteins have longer IDRs than the later actin polymerization- and scission-module proteins,[112] suggesting an evolutionary selection of IDR length to match protein functionality. Recently, the mammalian early modules Eps15 and Fcho1/2 were also found to undergo liquid-phase separation through weak interactions of IDRs to optimize endocytosis initiation.[113] Notably, the functions of IDRs are diverse and do not necessarily facilitate higher-order assembly by their unstructured nature. For example, certain IDRs may function only through conformational switching between static and disorder states.[114–116] Several ABPs are generally well folded and contain relatively shorter IDRs or loops, such as the capping protein fimbrin, the Arp2/3 complex, and cofilin.[112] A 27-aa IDR of yeast Sac6 regulates conformational flexibility between the N-terminal EF-hand domain and actin-binding domain 1 (ABD1) in a phosphorylation-dependent manner.[117,118] Although the IDRs of fimbrin homologs vary in sequence and length, the presence of an IDR and phosphorylation site is evolutionarily conserved among eukaryotic species.[117]

Here, we report another mechanism of IDRs, which optimizes CC oligomerization of Crn1 and thereby its actin patch localization and activities in F-actin cross-linking and inhibition of the Arp2/3 complex. In fact, IDRs are often located next to protein oligomerization domains, such as CC or prion-prone domains.[119–121] The CC domain contains multiple seven-residue heptad motifs and packs into parallel or antiparallel helical bundles through hydrophobic interactions.[61,62,65] The stability of α-helix assembly is the balanced result of interhelical interactions and depends on multiple determinants, including hydrophobic residues at the "a" and "d" positions, which constitute the hydrophobic core. In addition to this conventional topology, diverse packing geometries that do not necessarily follow classic heptad patterns exist.[62–66,122–128] We observed that the hydrophobic interaction between coronin CC helices is the dominant factor that contributes to the interhelical interactions and CC domain oligomerization. Crn1-CC is predicted to follow the classical seven-residue motif but contains two non-hydrophobic residues at the "a" and "d" positions that generate nonideal heptad repeats (Figure S2E). This may lead to unstable packing between helices with multiple relatively weak and heterogenic interactions between heptad repeats (Figure S5C), which in turn result in the high-order assembly of the CC (Figures 3B and 3D). The neighboring long IDR is then necessary to optimize the energy landscape of helix packing to prevent higher-order assemblies (Figures 3B, 3C, and 7G). The profound evolutionary selection of coronin IDRs with varied lengths could be influenced by how well the neighboring helical chains are packed. Coronins in higher species (e.g., mouse, human), in contrast, have evolved stable CCs (Figure 7C) with robust interhelical interactions, omitting the requirement of a long IDR to maintain an optimal energy level for a low-level oligomeric state (Figures 7D–7F, S5B, and S5E) and need only a short IDR for providing conformational flexibility for neighboring domains. However, with additional engineered Crn1 IDRs that vary in length but retain the same flexible residue repeats, we found that the specific amino acid composition also contributes to fine-tuning CC oligomerization, suggesting potential additional evolutionary selection pressures from binding partners of IDRs in a sequence-specific recognition-based manner, in addition to IDR length effects. In the future, the systems biology approach might reveal such a complex mechanism by which the coronin IDR or other IDRs will evolve through different combinations of oligomerization motif assembly energy, IDR length, and molecular grammar.

Limitations of the study

First, we purified Crn1 proteins from both *E. coli* and yeast and used analytical ultracentrifugation to determine their optimal tetrameric states. However, the tunable oligomerization common in nonequilibrium assemblies makes it difficult to quantify. These dynamic assemblies may respond to complex cellular environments, where interactions and modifications can affect the assembly energy landscape. Although we found a preferred oligomerization state for Crn1, we still have limited knowledge of intermediate species *in vivo* and their functions. Second, our research shows that IDRs play a significant role in protein function through various regulations such as conformational flexibility, length, and sequence. However, comparing the importance of different IDR features is challenging, as it depends on the surrounding functional domains. Third, we used MD simulations to gain insight into Crn1 and human Coronin 1A IDRs, but covering all coronins and their biochemical examinations is challenging. Moreover, the coarse-grained modeling approach used in this study to examine the oligomerization of CCs is mainly based on Ravikumar et al.[129] Although the intermolecular interactions in the model can be seen as a variation of the Kim-Hummer (KH) model,[130] which has been widely used in protein assembly modeling,[131] the model applied by Ravikumar et al.[129] was mainly focused on protein dimer complexes. In addition, both the model used in this study and the KH model rely on the Miyazawa-Jernigan (MJ) statistical potential to determine the strength of interactions between amino acid residues, while the MJ potential was derived from a relatively small dataset (1,168 crystal structures in the Protein Data Bank in 1996).[132] Considering these points, although we believe that the model

used in this work is reasonable, there is still room for improvement in the computational approach. Further verification is desirable to establish the model's general applicability to protein oligomerization.

STAR★METHODS

Detailed methods are provided in the online version of this paper and include the following:

- KEY RESOURCES TABLE
- RESOURCE AVAILABILITY
  - Lead contact
  - Materials availability
  - Data and code availability
- EXPERIMENTAL MODEL AND STUDY PARTICIPANT DETAILS
  - Mouse embryonic fibroblasts
  - *Saccharomyces cerevisiae* strains
- METHOD DETAILS
  - Yeast live-cell imaging
  - Yeast growth assay
  - Yeast whole-cell extraction and immunoblotting
  - MEF live-cell imaging
  - Protein expression and purification
  - Rabbit skeletal muscle actin (RMA) purification and labeling
  - Yeast protein expression and purification
  - Specimen preparation and transmission electron microscopy
  - Far-UV circular dichroism
  - Actin conversion assays
  - Total internal reflection fluorescence microscopy
  - Analytical ultracentrifugation (AUC)
  - Coronin sequence analysis and the taxonomic tree
  - Coarse-grained simulation
  - Langevin dynamics (LD) simulation
  - Data analysis
- QUANTIFICATION AND STATISTICAL ANALYSIS
  - mRuby2-patch intensity analysis
  - Cortex enrichment analysis of Coronin 1A in MEFs
  - Actin conversion analysis
  - Statistical analysis

SUPPLEMENTAL INFORMATION

Supplemental information can be found online at https://doi.org/10.1016/j.celrep.2023.112594.

ACKNOWLEDGMENTS

We thank the National Supercomputing Center Singapore (https://www.nscc.sg/) for assisting in the computational work. This study was supported by the Singapore Ministry of Education (MOE) Tier 3 (MOE2019-T3-1-012), MOE Tier 2 (MOE-T2EP30121-0015), and National Research Foundation Singapore under its Open Fund – Individual Research Grant (MOH-000955), and administered by the Singapore Ministry of Health's National Medical Research Council, to Y.M.; MOE Tier 1 (2018-T1-001-096) to L.L.; MOE Tier 1 (RT13/19) to J.T; and MOE Tier 3 (MOE2019-T3-1-012) to L.N.

AUTHOR CONTRIBUTIONS

X.H. and Y.M. conceived and designed this study. X.H. performed most of the wet lab experiments. Z.H. performed simulation work with help from F.Z. and under the guidance of L.L. and L.N. W.S. and X.H. performed the AUC experiments with guidance from J.T. Q.M. contributed to yeast genetic and imaging experiments. The manuscript was drafted by X.H. and Y.M. and received feedback from all authors. Y.M. supervised these studies.

DECLARATION OF INTERESTS

The authors declare no competing interests.

INCLUSION AND DIVERSITY

We support inclusive, diverse, and equitable conduct of research.

Received: October 18, 2022
Revised: April 21, 2023
Accepted: May 16, 2023
Published: June 1, 2023

REFERENCES

1. de Hostos, E.L., Bradtke, B., Lottspeich, F., Guggenheim, R., and Gerisch, G. (1991). Coronin, an actin binding protein of Dictyostelium discoideum localized to cell surface projections, has sequence similarities to G protein beta subunits. EMBO J. *10*, 4097–4104. https://doi.org/10.1002/j.1460-2075.1991.tb04986.x.
2. Uetrecht, A.C., and Bear, J.E. (2006). Coronins: the return of the crown. Trends Cell Biol. *16*, 421–426. https://doi.org/10.1016/j.tcb.2006.06.002.
3. de Hostos, E.L. (1999). The coronin family of actin-associated proteins. Trends Cell Biol. *9*, 345–350. https://doi.org/10.1016/s0962-8924(99)01620-7.
4. Okumura, M., Kung, C., Wong, S., Rodgers, M., and Thomas, M.L. (1998). Definition of family of coronin-related proteins conserved between humans and mice: close genetic linkage between coronin-2 and CD45-associated protein. DNA Cell Biol. *17*, 779–787. https://doi.org/10.1089/dna.1998.17.779.
5. Rybakin, V., and Clemen, C.S. (2005). Coronin proteins as multifunctional regulators of the cytoskeleton and membrane trafficking. Bioessays *27*, 625–632. https://doi.org/10.1002/bies.20235.
6. de Hostos, E.L. (2008). A Brief History of the Coronin Family. The Coronin Family of Proteins (Springer New York). https://doi.org/10.1007/978-0-387-09595-0_4.
7. Cai, L., Marshall, T.W., Uetrecht, A.C., Schafer, D.A., and Bear, J.E. (2007). Coronin 1B coordinates Arp2/3 complex and cofilin activities at the leading edge. Cell *128*, 915–929. https://doi.org/10.1016/j.cell.2007.01.031.
8. Cai, L., Makhov, A.M., Schafer, D.A., and Bear, J.E. (2008). Coronin 1B antagonizes cortactin and remodels Arp2/3-containing actin branches in lamellipodia. Cell *134*, 828–842. https://doi.org/10.1016/j.cell.2008.06.054.
9. Cai, L., Holoweckyj, N., Schaller, M.D., and Bear, J.E. (2005). Phosphorylation of coronin 1B by protein kinase C regulates interaction with Arp2/3 and cell motility. J. Biol. Chem. *280*, 31913–31923. https://doi.org/10.1074/jbc.M504146200.
10. Cai, L., Makhov, A.M., and Bear, J.E. (2007). F-actin binding is essential for coronin 1B function in vivo. J. Cell Sci. *120*, 1779–1790. https://doi.org/10.1242/jcs.007641.
11. Samarin, S.N., Koch, S., Ivanov, A.I., Parkos, C.A., and Nusrat, A. (2010). Coronin 1C negatively regulates cell-matrix adhesion and motility of intestinal epithelial cells. Biochem. Biophys. Res. Commun. *391*, 394–400. https://doi.org/10.1016/j.bbrc.2009.11.069.

12. Marshall, T.W., Aloor, H.L., and Bear, J.E. (2009). Coronin 2A regulates a subset of focal-adhesion-turnover events through the cofilin pathway. J. Cell Sci. *122*, 3061–3069. https://doi.org/10.1242/jcs.051482.

13. Ishikawa-Ankerhold, H.C., Gerisch, G., and Müller-Taubenberger, A. (2010). Genetic evidence for concerted control of actin dynamics in cytokinesis, endocytic traffic, and cell motility by coronin and Aip1. Cytoskeleton *67*, 442–455. https://doi.org/10.1002/cm.20456.

14. Mishima, M., and Nishida, E. (1999). Coronin localizes to leading edges and is involved in cell spreading and lamellipodium extension in vertebrate cells. J. Cell Sci. *112*, 2833–2842. https://doi.org/10.1242/jcs.112.17.2833.

15. de Hostos, E.L., Rehfuess, C., Bradtke, B., Waddell, D.R., Albrecht, R., Murphy, J., and Gerisch, G. (1993). Dictyostelium mutants lacking the cytoskeletal protein coronin are defective in cytokinesis and cell motility. J. Cell Biol. *120*, 163–173. https://doi.org/10.1083/jcb.120.1.163.

16. Kimura, T., Kaneko, Y., Yamada, S., Ishihara, H., Senda, T., Iwamatsu, A., and Niki, I. (2008). The GDP-dependent Rab27a effector coronin 3 controls endocytosis of secretory membrane in insulin-secreting cell lines. J. Cell Sci. *121*, 3092–3098. https://doi.org/10.1242/jcs.030544.

17. Echauri-Espinosa, R.O., Callejas-Negrete, O.A., Roberson, R.W., Bartnicki-García, S., and Mouriño-Pérez, R.R. (2012). Coronin is a component of the endocytic collar of hyphae of neurospora crassa and is necessary for normal growth and morphogenesis. PLoS One *7*, e38237. https://doi.org/10.1371/journal.pone.0038237.

18. Yan, M., Collins, R.F., Grinstein, S., and Trimble, W.S. (2005). Coronin-1 function is required for phagosome formation. Mol. Biol. Cell *16*, 3077–3087. https://doi.org/10.1091/mbc.e04-11-0989.

19. Maniak, M., Rauchenberger, R., Albrecht, R., Murphy, J., and Gerisch, G. (1995). Coronin involved in phagocytosis: dynamics of particle-induced relocalization visualized by a green fluorescent protein tag. Cell *83*, 915–924. https://doi.org/10.1016/0092-8674(95)90207-4.

20. Huang, W., Ghisletti, S., Saijo, K., Gandhi, M., Aouadi, M., Tesz, G.J., Zhang, D.X., Yao, J., Czech, M.P., Goode, B.L., et al. (2011). Coronin 2A mediates actin-dependent de-repression of inflammatory response genes. Nature *470*, 414–418. https://doi.org/10.1038/nature09703.

21. Föger, N., Rangell, L., Danilenko, D.M., and Chan, A.C. (2006). Requirement for coronin 1 in T lymphocyte trafficking and cellular homeostasis. Science *313*, 839–842. https://doi.org/10.1126/science.1130563.

22. Shiow, L.R., Roadcap, D.W., Paris, K., Watson, S.R., Grigorova, I.L., Lebet, T., An, J., Xu, Y., Jenne, C.N., Föger, N., et al. (2008). The actin regulator coronin 1A is mutant in a thymic egress-deficient mouse strain and in a patient with severe combined immunodeficiency. Nat. Immunol. *9*, 1307–1315. https://doi.org/10.1038/ni.1662.

23. Mueller, P., Massner, J., Jayachandran, R., Combaluzier, B., Albrecht, I., Gatfield, J., Blum, C., Ceredig, R., Rodewald, H.R., Rolink, A.G., and Pieters, J. (2008). Regulation of T cell survival through coronin-1-mediated generation of inositol-1,4,5-trisphosphate and calcium mobilization after T cell receptor triggering. Nat. Immunol. *9*, 424–431. https://doi.org/10.1038/ni1570.

24. Pieters, J., Müller, P., and Jayachandran, R. (2013). On guard: coronin proteins in innate and adaptive immunity. Nat. Rev. Immunol. *13*, 510–518. https://doi.org/10.1038/nri3465.

25. Brieher, W.M., Kueh, H.Y., Ballif, B.A., and Mitchison, T.J. (2006). Rapid actin monomer–insensitive depolymerization of Listeria actin comet tails by cofilin, coronin, and Aip1. J. Cell Biol. *175*, 315–324. https://doi.org/10.1083/jcb.200603149.

26. Lin, M.C., Galletta, B.J., Sept, D., and Cooper, J.A. (2010). Overlapping and distinct functions for cofilin, coronin and Aip1 in actin dynamics in vivo. J. Cell Sci. *123*, 1329–1342. https://doi.org/10.1242/jcs.065698.

27. Humphries, C.L., Balcer, H.I., D'Agostino, J.L., Winsor, B., Drubin, D.G., Barnes, G., Andrews, B.J., and Goode, B.L. (2002). Direct regulation of Arp2/3 complex activity and function by the actin binding protein coronin. J. Cell Biol. *159*, 993–1004. https://doi.org/10.1083/jcb.200206113.

28. Rodal, A.A., Sokolova, O., Robins, D.B., Daugherty, K.M., Hippenmeyer, S., Riezman, H., Grigorieff, N., and Goode, B.L. (2005). Conformational changes in the Arp2/3 complex leading to actin nucleation. Nat. Struct. Mol. Biol. *12*, 26–31. https://doi.org/10.1038/nsmb870.

29. Sokolova, O.S., Chemeris, A., Guo, S., Alioto, S.L., Gandhi, M., Padrick, S., Pechnikova, E., David, V., Gautreau, A., and Goode, B.L. (2017). Structural basis of arp2/3 complex inhibition by GMF, coronin, and arpin. J. Mol. Biol. *429*, 237–248. https://doi.org/10.1016/j.jmb.2016.11.030.

30. Goode, B.L., Wong, J.J., Butty, A.-C., Peter, M., McCormack, A.L., Yates, J.R., Drubin, D.G., and Barnes, G. (1999). Coronin promotes the rapid assembly and cross-linking of actin filaments and may link the actin and microtubule cytoskeletons in yeast. J. Cell Biol. *144*, 83–98. https://doi.org/10.1083/jcb.144.1.83.

31. Liu, C.Z., Chen, Y., and Sui, S.F. (2006). The identification of a new actin-binding region in p57. Cell Res. *16*, 106–112. https://doi.org/10.1038/sj.cr.7310014.

32. Gandhi, M., Achard, V., Blanchoin, L., and Goode, B.L. (2009). Coronin switches roles in actin disassembly depending on the nucleotide state of actin. Mol. Cell *34*, 364–374. https://doi.org/10.1016/j.molcel.2009.02.029.

33. Tang, V.W., Nadkarni, A.V., and Brieher, W.M. (2020). Catastrophic actin filament bursting by cofilin, Aip1, and coronin. J. Biol. Chem. *295*, 13299–13313. https://doi.org/10.1074/jbc.RA120.015018.

34. Kueh, H.Y., Charras, G.T., Mitchison, T.J., and Brieher, W.M. (2008). Actin disassembly by cofilin, coronin, and Aip1 occurs in bursts and is inhibited by barbed-end cappers. J. Cell Biol. *182*, 341–353. https://doi.org/10.1083/jcb.200801027.

35. Mikati, M.A., Breitsprecher, D., Jansen, S., Reisler, E., and Goode, B.L. (2015). Coronin enhances actin filament severing by recruiting cofilin to filament sides and altering F-actin conformation. J. Mol. Biol. *427*, 3137–3147. https://doi.org/10.1016/j.jmb.2015.08.011.

36. Gandhi, M., Jangi, M., and Goode, B.L. (2010). Functional surfaces on the actin-binding protein coronin revealed by systematic mutagenesis. J. Biol. Chem. *285*, 34899–34908. https://doi.org/10.1074/jbc.M110.171496.

37. Galkin, V.E., Orlova, A., Brieher, W., Kueh, H.Y., Mitchison, T.J., and Egelman, E.H. (2008). Coronin-1A stabilizes F-actin by bridging adjacent actin protomers and stapling opposite strands of the actin filament. J. Mol. Biol. *376*, 607–613. https://doi.org/10.1016/j.jmb.2007.12.007.

38. Appleton, B.A., Wu, P., and Wiesmann, C. (2006). The crystal structure of murine coronin-1: a regulator of actin cytoskeletal dynamics in lymphocytes. Structure *14*, 87–96. https://doi.org/10.1016/j.str.2005.09.013.

39. Oku, T., Itoh, S., Okano, M., Suzuki, A., Suzuki, K., Nakajin, S., Tsuji, T., Nauseef, W.M., and Toyoshima, S. (2003). Two regions responsible for the actin binding of p57, a mammalian coronin family actin-binding protein. Biol. Pharm. Bull. *26*, 409–416. https://doi.org/10.1248/bpb.26.409.

40. Chan, K.T., Roadcap, D.W., Holoweckyj, N., and Bear, J.E. (2012). Coronin 1C harbours a second actin-binding site that confers co-operative binding to F-actin. Biochem. J. *444*, 89–96. https://doi.org/10.1042/BJ20120209.

41. Rosentreter, A., Hofmann, A., Xavier, C.P., Stumpf, M., Noegel, A.A., and Clemen, C.S. (2007). Coronin 3 involvement in F-actin-dependent processes at the cell cortex. Exp. Cell Res. *313*, 878–895. https://doi.org/10.1016/j.yexcr.2006.12.015.

42. Spoerl, Z., Stumpf, M., Noegel, A.A., and Hasse, A. (2002). Oligomerization, F-actin interaction, and membrane association of the ubiquitous mammalian coronin 3 are mediated by its carboxyl terminus. J. Biol. Chem. *277*, 48858–48867. https://doi.org/10.1074/jbc.M205136200.

43. Gatfield, J., Albrecht, I., Zanolari, B., Steinmetz, M.O., and Pieters, J. (2005). Association of the leukocyte plasma membrane with the actin

cytoskeleton through coiled coil-mediated trimeric coronin 1 molecules. Mol. Biol. Cell *16*, 2786–2798. https://doi.org/10.1091/mbc.E05-01-0042.

44. Oku, T., Itoh, S., Ishii, R., Suzuki, K., Nauseef, W.M., Toyoshima, S., and Tsuji, T. (2005). Homotypic dimerization of the actin-binding protein p57/coronin-1 mediated by a leucine zipper motif in the C-terminal region. Biochem. J. *387*, 325–331. https://doi.org/10.1042/bj20041020.
45. Asano, S., Mishima, M., and Nishida, E. (2001). Coronin forms a stable dimer through its C-terminal coiled coil region: an implicated role in its localization to cell periphery. Gene Cell. *6*, 225–235. https://doi.org/10.1046/j.1365-2443.2001.00416.x.
46. Nayak, A.R., Karade, S.S., Srivastava, V.K., Rana, A.K., Gupta, C.M., Sahasrabuddhe, A.A., and Pratap, J.V. (2016). Structure of Leishmania donovani coronin coiled coil domain reveals an antiparallel 4 helix bundle with inherent asymmetry. J. Struct. Biol. *195*, 129–138. https://doi.org/10.1016/j.jsb.2016.02.020.
47. Kammerer, R.A., Kostrewa, D., Progias, P., Honnappa, S., Avila, D., Lustig, A., Winkler, F.K., Pieters, J., and Steinmetz, M.O. (2005). A conserved trimerization motif controls the topology of short coiled coils. Proc. Natl. Acad. Sci. USA *102*, 13891–13896. https://doi.org/10.1073/pnas.0502390102.
48. Salamun, J., Kallio, J.P., Daher, W., Soldati-Favre, D., and Kursula, I. (2014). Structure of Toxoplasma gondii coronin, an actin-binding protein that relocalizes to the posterior pole of invasive parasites and contributes to invasion and egress. Faseb. J. *28*, 4729–4747. https://doi.org/10.1096/fj.14-252569.
49. Liu, S.L., Needham, K.M., May, J.R., and Nolen, B.J. (2011). Mechanism of a concentration-dependent switch between activation and inhibition of Arp2/3 complex by coronin. J. Biol. Chem. *286*, 17039–17046. https://doi.org/10.1074/jbc.M111.219964.
50. Srivastava, R., Prasadareddy Kajuluri, L., Pathak, N., Gupta, C.M., and Sahasrabuddhe, A.A. (2015). Oligomerization of coronin: implication on actin filament length in Leishmania. Cytoskeleton *72*, 621–632. https://doi.org/10.1002/cm.21269.
51. Heil-Chapdelaine, R.A., Tran, N.K., and Cooper, J.A. (1998). The role of Saccharomyces cerevisiae coronin in the actin and microtubule cytoskeletons. Curr. Biol. *8*, 1281–1284. https://doi.org/10.1016/S0960-9822(07)00539-8.
52. Mészáros, B., Erdos, G., and Dosztányi, Z. (2018). IUPred2A: context-dependent prediction of protein disorder as a function of redox state and protein binding. Nucleic Acids Res. *46*, W329–W337. https://doi.org/10.1093/nar/gky384.
53. Erdős, G., and Dosztányi, Z. (2020). Analyzing protein disorder with IUPred2A. Curr. Protoc. Bioinformatics *70*, e99. https://doi.org/10.1002/cpbi.99.
54. Ludwiczak, J., Winski, A., Szczepaniak, K., Alva, V., and Dunin-Horkawicz, S. (2019). DeepCoil-a fast and accurate prediction of coiled-coil domains in protein sequences. Bioinformatics *35*, 2790–2795. https://doi.org/10.1093/bioinformatics/bty1062.
55. Ge, P., Durer, Z.A.O., Kudryashov, D., Zhou, Z.H., and Reisler, E. (2014). Cryo-EM reveals different coronin binding modes for ADP- and ADP-BeFx actin filaments. Nat. Struct. Mol. Biol. *21*, 1075–1081. https://doi.org/10.1038/nsmb.2907.
56. Dalgleish, D.G. (1972). The analysis of the far-ultraviolet circular dichroism spectra of proteins. FEBS Lett. *24*, 134–136. https://doi.org/10.1016/0014-5793(72)80844-5.
57. Greenfield, N.J. (2006). Using circular dichroism spectra to estimate protein secondary structure. Nat. Protoc. *1*, 2876–2890. https://doi.org/10.1038/nprot.2006.202.
58. Kelly, S.M., and Price, N.C. (2000). The use of circular dichroism in the investigation of protein structure and function. Curr. Protein Pept. Sci. *1*, 349–384. https://doi.org/10.2174/1389203003381315.
59. Crick, F.H.C. (1952). Is alpha-keratin a coiled coil? Nature *170*, 882–883. https://doi.org/10.1038/170882b0.
60. Crick, F.H.C. (1953). The Fourier transform of a coiled-coil. Acta Crystallogr. *6*, 685–689. https://doi.org/10.1107/S0365110X53001952.
61. Lupas, A. (1996). Coiled coils: new structures and new functions. Trends Biochem. Sci. *21*, 375–382. https://doi.org/10.1016/S0968-0004(96)10052-9.
62. Lupas, A.N., and Gruber, M. (2005). The structure of α-helical coiled coils. Advances in Protein Chemistry (Academic Press). https://doi.org/10.1016/S0065-3233(05)70003-6.
63. Grigoryan, G., and Keating, A.E. (2008). Structural specificity in coiled-coil interactions. Curr. Opin. Struct. Biol. *18*, 477–483. https://doi.org/10.1016/j.sbi.2008.04.008.
64. Apostolovic, B., Danial, M., and Klok, H.A. (2010). Coiled coils: attractive protein folding motifs for the fabrication of self-assembled, responsive and bioactive materials. Chem. Soc. Rev. *39*, 3541–3575. https://doi.org/10.1039/b914339b.
65. Lupas, A.N., Bassler, J., and Dunin-Horkawicz, S. (2017). The Structure and Topology of α-Helical Coiled Coils. Subcellular Biochemistry (Springer). https://doi.org/10.1007/978-3-319-49674-0_4.
66. Woolfson, D.N. (2005). The design of coiled-coil structures and assemblies. Advances in Protein Chemistry (Academic Press). https://doi.org/10.1016/s0065-3233(05)70004-8.
67. Li, C., Ching Han Chang, C., Nagel, J., Porebski, B.T., Hayashida, M., Akutsu, T., Song, J., and Buckle, A.M. (2016). Critical evaluation of in silico methods for prediction of coiled-coil domains in proteins. Brief. Bioinform. *17*, 270–282. https://doi.org/10.1093/bib/bbv047.
68. Schirò, G., Fichou, Y., Gallat, F.-X., Wood, K., Gabel, F., Moulin, M., Härtlein, M., Heyden, M., Colletier, J.-P., Orecchini, A., et al. (2015). Translational diffusion of hydration water correlates with functional motions in folded and intrinsically disordered proteins. Nat. Commun. *6*, 6490. https://doi.org/10.1038/ncomms7490.
69. Xie, Y., Han, X., and Miao, Y. (2018). An effective recombinant protein expression and purification system in Saccharomyces cerevisiae. Curr. Protoc. Mol. Biol. *123*, e62. https://doi.org/10.1002/cpmb.62.
70. Khairil Anuar, I.N.A., Banerjee, A., Keeble, A.H., Carella, A., Nikov, G.I., and Howarth, M. (2019). Spy&Go purification of SpyTag-proteins using pseudo-SpyCatcher to access an oligomerization toolbox. Nat. Commun. *10*, 1734. https://doi.org/10.1038/s41467-019-09678-w.
71. Kühnel, K., Jarchau, T., Wolf, E., Schlichting, I., Walter, U., Wittinghofer, A., and Strelkov, S.V. (2004). The VASP tetramerization domain is a right-handed coiled coil based on a 15-residue repeat. Proc. Natl. Acad. Sci. USA *101*, 17027–17032. https://doi.org/10.1073/pnas.0403069101.
72. Fletcher, J.M., Boyle, A.L., Bruning, M., Bartlett, G.J., Vincent, T.L., Zaccai, N.R., Armstrong, C.T., Bromley, E.H.C., Booth, P.J., Brady, R.L., et al. (2012). A basis set of de Novo coiled-coil peptide oligomers for rational protein design and synthetic biology. ACS Synth. Biol. *1*, 240–250. https://doi.org/10.1021/sb300028q.
73. Malashkevich, V.N., Kammerer, R.A., Efimov, V.P., Schulthess, T., and Engel, J. (1996). The crystal structure of a five-stranded coiled coil in COMP: a prototype ion channel? Science *274*, 761–765. https://doi.org/10.1126/science.274.5288.761.
74. Li, Z., Vizeacoumar, F.J., Bahr, S., Li, J., Warringer, J., Vizeacoumar, F.S., Min, R., VanderSluis, B., Bellay, J., DeVit, M., et al. (2011). Systematic exploration of essential yeast gene function with temperature-sensitive mutants. Nat. Biotechnol. *29*, 361–367. https://doi.org/10.1038/nbt.1832.
75. Sun, H., Zhu, X., Li, C., Ma, Z., Han, X., Luo, Y., Yang, L., Yu, J., and Miao, Y. (2021). Xanthomonas effector XopR hijacks host actin cytoskeleton via complex coacervation. Nat. Commun. *12*, 4064. https://doi.org/10.1038/s41467-021-24375-3.
76. Skau, C.T., Courson, D.S., Bestul, A.J., Winkelman, J.D., Rock, R.S., Sirotkin, V., and Kovar, D.R. (2011). Actin filament bundling by fimbrin is important for endocytosis, cytokinesis, and polarization in fission yeast.

J. Biol. Chem. *286*, 26964–26977. https://doi.org/10.1074/jbc.M111.239004.

77. Allwood, E.G., Tyler, J.J., Urbanek, A.N., Smaczynska-de Rooij, I.I., Ayscough, K.R., and Ayscough, K.R. (2016). Elucidating key motifs required for arp2/3-dependent and independent actin nucleation by Las17/WASP. PLoS One *11*, e0163177. https://doi.org/10.1371/journal.pone.0163177.
78. Eckert, C., Hammesfahr, B., and Kollmar, M. (2011). A holistic phylogeny of the coronin gene family reveals an ancient origin of the tandem-coronin, defines a new subfamily, and predicts protein function. BMC Evol. Biol. *11*, 268. https://doi.org/10.1186/1471-2148-11-268.
79. Kastano, K., Erdős, G., Mier, P., Alanis-Lobato, G., Promponas, V.J., Dosztányi, Z., and Andrade-Navarro, M.A. (2020). Evolutionary study of disorder in protein sequences. Biomolecules *10*, 1413. https://doi.org/10.3390/biom10101413.
80. Ward, J.J., Sodhi, J.S., McGuffin, L.J., Buxton, B.F., and Jones, D.T. (2004). Prediction and functional analysis of native disorder in proteins from the three kingdoms of life. J. Mol. Biol. *337*, 635–645. https://doi.org/10.1016/j.jmb.2004.02.002.
81. Letunic, I., and Bork, P. (2019). Interactive Tree of Life (iTOL) v4: recent updates and new developments. Nucleic Acids Res. *47*, W256–W259. https://doi.org/10.1093/nar/gkz239.
82. Rotkiewicz, P., and Skolnick, J. (2008). Fast procedure for reconstruction of full-atom protein models from reduced representations. J. Comput. Chem. *29*, 1460–1465. https://doi.org/10.1002/jcc.20906.
83. Pollard, T.D. (2016). Actin and actin-binding proteins. Cold Spring Harbor Perspect. Biol. *8*, a018226. https://doi.org/10.1101/cshperspect.a018226.
84. Lee, S.H., and Dominguez, R. (2010). Regulation of actin cytoskeleton dynamics in cells. Mol. Cells *29*, 311–325. https://doi.org/10.1007/s10059-010-0053-8.
85. Dos Remedios, C.G., Chhabra, D., Kekic, M., Dedova, I.V., Tsubakihara, M., Berry, D.A., and Nosworthy, N.J. (2003). Actin binding proteins: regulation of cytoskeletal microfilaments. Physiol. Rev. *83*, 433–473. https://doi.org/10.1152/physrev.00026.2002.
86. Xu, Y., Moseley, J.B., Sagot, I., Poy, F., Pellman, D., Goode, B.L., and Eck, M.J. (2004). Crystal structures of a formin homology-2 domain reveal a tethered dimer architecture. Cell *116*, 711–723. https://doi.org/10.1016/S0092-8674(04)00210-7.
87. Goode, B.L., and Eck, M.J. (2007). Mechanism and function of formins in the control of actin assembly. Annu. Rev. Biochem. *76*, 593–627. https://doi.org/10.1146/annurev.biochem.75.103004.142647.
88. Pollard, T.D. (2007). Regulation of actin filament assembly by Arp2/3 complex and formins. Annu. Rev. Biophys. *36*, 451–477. https://doi.org/10.1146/annurev.biophys.35.040405.101936.
89. Nitanai, Y., Minakata, S., Maeda, K., Oda, N., and Maéda, Y. (2007). Crystal structures of tropomyosin: flexible coiled-coil. Regulatory Mechanisms of Striated Muscle Contraction (Springer Japan). https://doi.org/10.1007/978-4-431-38453-3_13.
90. Gordon, A.M., Homsher, E., and Regnier, M. (2000). Regulation of contraction in striated muscle. Physiol. Rev. *80*, 853–924. https://doi.org/10.1152/physrev.2000.80.2.853.
91. Drees, B., Brown, C., Barrell, B.G., and Bretscher, A. (1995). Tropomyosin is essential in yeast, yet the TPM1 and TPM2 products perform distinct functions. J. Cell Biol. *128*, 383–392. https://doi.org/10.1083/jcb.128.3.383.
92. Shen, K., Tolbert, C.E., Guilluy, C., Swaminathan, V.S., Berginski, M.E., Burridge, K., Superfine, R., and Campbell, S.L. (2011). The vinculin C-terminal hairpin mediates F-actin bundle formation, focal adhesion, and cell mechanical properties. J. Biol. Chem. *286*, 45103–45115. https://doi.org/10.1074/jbc.M111.244293.
93. Thompson, P.M., Tolbert, C.E., and Campbell, S.L. (2013). Vinculin and metavinculin: oligomerization and interactions with F-actin. FEBS Lett. *587*, 1220–1229. https://doi.org/10.1016/j.febslet.2013.02.042.
94. Sun, H., Qiao, Z., Chua, K.P., Tursic, A., Liu, X., Gao, Y.G., Mu, Y., Hou, X., and Miao, Y. (2018). Profilin negatively regulates formin-mediated actin assembly to modulate PAMP-triggered plant immunity. Curr. Biol. *28*, 1882–1895.e7. https://doi.org/10.1016/j.cub.2018.04.045.
95. Xie, Y., Sun, J., Han, X., Turšić-Wunder, A., Toh, J.D.W., Hong, W., Gao, Y.G., and Miao, Y. (2019). Polarisome scaffolder Spa2-mediated macromolecular condensation of Aip5 for actin polymerization. Nat. Commun. *10*, 5078. https://doi.org/10.1038/s41467-019-13125-1.
96. Qiao, Z., Sun, H., Ng, J.T.Y., Ma, Q., Koh, S.H., Mu, Y., Miao, Y., and Gao, Y.-G. (2019). Structural and computational examination of the Arabidopsis profilin-Poly-P complex reveals mechanistic details in profilin-regulated actin assembly. J. Biol. Chem. *294*, 18650–18661. https://doi.org/10.1074/jbc.RA119.011307.
97. Xie, Y., Loh, Z.Y., Xue, J., Zhou, F., Sun, J., Qiao, Z., Jin, S., Deng, Y., Li, H., Wang, Y., et al. (2020). Orchestrated actin nucleation by the Candida albicans polarisome complex enables filamentous growth. J. Biol. Chem. *295*, 14840–14854. https://doi.org/10.1074/jbc.RA120.013890.
98. Xie, Y., and Miao, Y. (2021). Polarisome assembly mediates actin remodeling during polarized yeast and fungal growth. J. Cell Sci. *134*, jcs247916. https://doi.org/10.1242/jcs.247916.
99. Ma, Z., Sun, Y., Zhu, X., Yang, L., Chen, X., and Miao, Y. (2022). Membrane nanodomains modulate formin condensation for actin remodeling in Arabidopsis innate im-mune responses. Plant Cell *34*, 374–394. https://doi.org/10.1093/plcell/koab261.
100. Ma, Z., Liu, X., Nath, S., Sun, H., Tran, T.M., Yang, L., Mayor, S., and Miao, Y. (2021). Formin nanoclustering-mediated actin assembly during plant flagellin and DSF signaling. Cell Rep. *34*, 108884. https://doi.org/10.1016/j.celrep.2021.108884.
101. Padrick, S.B., Doolittle, L.K., Brautigam, C.A., King, D.S., and Rosen, M.K. (2011). Arp2/3 complex is bound and activated by two WASP proteins. Proc. Natl. Acad. Sci. USA *108*, E472–E479. https://doi.org/10.1073/pnas.1100236108.
102. Su, X., Ditlev, J.A., Hui, E., Xing, W., Banjade, S., Okrut, J., King, D.S., Taunton, J., Rosen, M.K., and Vale, R.D. (2016). Phase separation of signaling molecules promotes T cell receptor signal transduction. Science *352*, 595–599. https://doi.org/10.1126/science.aad9964.
103. Case, L.B., Zhang, X., Ditlev, J.A., and Rosen, M.K. (2019). Stoichiometry controls activity of phase-separated clusters of actin signaling proteins. Science *363*, 1093–1097. https://doi.org/10.1126/science.aau6313.
104. Wen, K.-K., Rubenstein, P.A., and DeMali, K.A. (2009). Vinculin nucleates actin polymerization and modifies actin filament structure. J. Biol. Chem. *284*, 30463–30473. https://doi.org/10.1074/jbc.M109.021295.
105. Breitsprecher, D., Kiesewetter, A.K., Linkner, J., Vinzenz, M., Stradal, T.E.B., Small, J.V., Curth, U., Dickinson, R.B., and Faix, J. (2011). Molecular mechanism of Ena/VASP-mediated actin-filament elongation. EMBO J. *30*, 456–467. https://doi.org/10.1038/emboj.2010.348.
106. Brühmann, S., Ushakov, D.S., Winterhoff, M., Dickinson, R.B., Curth, U., and Faix, J. (2017). Distinct VASP tetramers synergize in the processive elongation of individual actin filaments from clustered arrays. Proc. Natl. Acad. Sci. USA *114*, E5815–E5824. https://doi.org/10.1073/pnas.1703145114.
107. Bays, J.L., and DeMali, K.A. (2017). Vinculin in cell-cell and cell-matrix adhesions. Cell. Mol. Life Sci. *74*, 2999–3009. https://doi.org/10.1007/s00018-017-2511-3.
108. Rothenberg, M.E., Rogers, S.L., Vale, R.D., Jan, L.Y., and Jan, Y.N. (2003). Drosophila pod-1 crosslinks both actin and microtubules and controls the targeting of axons. Neuron *39*, 779–791. https://doi.org/10.1016/s0896-6273(03)00508-7.
109. van der Lee, R., Buljan, M., Lang, B., Weatheritt, R.J., Daughdrill, G.W., Dunker, A.K., Fuxreiter, M., Gough, J., Gsponer, J., Jones, D.T., et al. (2014). Classification of intrinsically disordered regions and proteins. Chem. Rev. *114*, 6589–6631. https://doi.org/10.1021/cr400525m.

110. Fung, H.Y.J., Birol, M., and Rhoades, E. (2018). IDPs in macromolecular complexes: the roles of multivalent interactions in diverse assemblies. Curr. Opin. Struct. Biol. *49*, 36–43. https://doi.org/10.1016/j.sbi.2017.12.007.

111. Wu, H., and Fuxreiter, M. (2016). The structure and dynamics of higher-order assemblies: amyloids, signalosomes, and granules. Cell *165*, 1055–1066. https://doi.org/10.1016/j.cell.2016.05.004.

112. Miao, Y., Tipakornsaowapak, T., Zheng, L., Mu, Y., and Lewellyn, E. (2018). Phospho-regulation of intrinsically disordered proteins for actin assembly and endocytosis. FEBS J. *285*, 2762–2784. https://doi.org/10.1111/febs.14493.

113. Day, K.J., Kago, G., Wang, L., Richter, J.B., Hayden, C.C., Lafer, E.M., and Stachowiak, J.C. (2021). Liquid-like protein interactions catalyse assembly of endocytic vesicles. Nat. Cell Biol. *23*, 366–376. https://doi.org/10.1038/s41556-021-00646-5.

114. Tompa, P., and Fuxreiter, M. (2008). Fuzzy complexes: polymorphism and structural disorder in protein-protein interactions. Trends Biochem. Sci. *33*, 2–8. https://doi.org/10.1016/j.tibs.2007.10.003.

115. Babu, M.M., Kriwacki, R.W., and Pappu, R.V. (2012). Structural biology. Versatility from protein disorder. Science *337*, 1460–1461. https://doi.org/10.1126/science.1228775.

116. Dyson, H.J., and Wright, P.E. (2005). Intrinsically unstructured proteins and their functions. Nat. Rev. Mol. Cell Biol. *6*, 197–208. https://doi.org/10.1038/nrm1589.

117. Miao, Y., Han, X., Zheng, L., Xie, Y., Mu, Y., Yates, J.R., 3rd, and Drubin, D.G. (2016). Fimbrin phosphorylation by metaphase Cdk1 regulates actin cable dynamics in budding yeast. Nat. Commun. *7*, 11265. https://doi.org/10.1038/ncomms11265.

118. Miao, Y., Wong, C.C.L., Mennella, V., Michelot, A., Agard, D.A., Holt, L.J., Yates, J.R., 3rd, and Drubin, D.G. (2013). Cell-cycle regulation of formin-mediated actin cable assembly. Proc. Natl. Acad. Sci. USA *110*, E4446–E4455. https://doi.org/10.1073/pnas.1314000110.

119. Anurag, M., Singh, G.P., and Dash, D. (2012). Location of disorder in coiled coil proteins is influenced by its biological role and subcellular localization: a GO-based study on human proteome. Mol. Biosyst. *8*, 346–352. https://doi.org/10.1039/c1mb05210a.

120. Fong, J.H., Shoemaker, B.A., Garbuzynskiy, S.O., Lobanov, M.Y., Galzitskaya, O.V., and Panchenko, A.R. (2009). Intrinsic disorder in protein interactions: insights from a comprehensive structural analysis. PLoS Comput. Biol. *5*, e1000316. https://doi.org/10.1371/journal.pcbi.1000316.

121. Malinovska, L., Kroschwald, S., and Alberti, S. (2013). Protein disorder, prion propensities, and self-organizing macromolecular collectives. Biochim. Biophys. Acta *1834*, 918–931. https://doi.org/10.1016/j.bbapap.2013.01.003.

122. Ciani, B., Bjelic, S., Honnappa, S., Jawhari, H., Jaussi, R., Payapilly, A., Jowitt, T., Steinmetz, M.O., and Kammerer, R.A. (2010). Molecular basis of coiled-coil oligomerization-state specificity. Proc. Natl. Acad. Sci. USA *107*, 19850–19855. https://doi.org/10.1073/pnas.1008502107.

123. Yadav, M.K., Leman, L.J., Price, D.J., Brooks, C.L., 3rd, Stout, C.D., and Ghadiri, M.R. (2006). Coiled coils at the edge of configurational heterogeneity. Structural analyses of parallel and antiparallel homotetrameric coiled coils reveal configurational sensitivity to a single solvent-exposed amino acid substitution. Biochemistry *45*, 4463–4473. https://doi.org/10.1021/bi060092q.

124. Liu, J., Zheng, Q., Deng, Y., Cheng, C.-S., Kallenbach, N.R., and Lu, M. (2006). A seven-helix coiled coil. Proc. Natl. Acad. Sci. USA *103*, 15457–15462. https://doi.org/10.1073/pnas.0604871103.

125. Hicks, M.R., Walshaw, J., and Woolfson, D.N. (2002). Investigating the tolerance of coiled-coil peptides to nonheptad sequence inserts. J. Struct. Biol. *137*, 73–81. https://doi.org/10.1006/jsbi.2002.4462.

126. Hicks, M.R., Holberton, D.V., Kowalczyk, C., and Woolfson, D.N. (1997). Coiled-coil assembly by peptides with non-heptad sequence motifs. Fold. Des. *2*, 149–158. https://doi.org/10.1016/s1359-0278(97)00021-7.

127. Harbury, P.B., Zhang, T., Kim, P.S., and Alber, T. (1993). A switch between two-three-and four-stranded coiled coils in GCN4 leucine zipper mutants. Science *262*, 1401–1407. https://doi.org/10.1126/science.8248779.

128. Keating, A.E., Malashkevich, V.N., Tidor, B., and Kim, P.S. (2001). Side-chain repacking calculations for predicting structures and stabilities of heterodimeric coiled coils. Proc. Natl. Acad. Sci. USA *98*, 14825–14830. https://doi.org/10.1073/pnas.261563398.

129. Ravikumar, K.M., Huang, W., and Yang, S. (2012). Coarse-grained simulations of protein-protein association: an energy landscape perspective. Biophys. J. *103*, 837–845. https://doi.org/10.1016/j.bpj.2012.07.013.

130. Kim, Y.C., and Hummer, G. (2008). Coarse-grained models for simulations of multiprotein complexes: application to ubiquitin binding. J. Mol. Biol. *375*, 1416–1433. https://doi.org/10.1016/j.jmb.2007.11.063.

131. Dignon, G.L., Zheng, W., Kim, Y.C., Best, R.B., and Mittal, J. (2018). Sequence determinants of protein phase behavior from a coarse-grained model. PLoS Comput. Biol. *14*, e1005941. https://doi.org/10.1371/journal.pcbi.1005941.

132. Miyazawa, S., and Jernigan, R.L. (1996). Residue-residue potentials with a favorable contact pair term and an unfavorable high packing density term, for simulation and threading. J. Mol. Biol. *256*, 623–644. https://doi.org/10.1006/jmbi.1996.0114.

133. Kalia, M., Kumari, S., Chadda, R., Hill, M.M., Parton, R.G., and Mayor, S. (2006). Arf6-independent GPI-anchored protein-enriched early endosomal compartments fuse with sorting endosomes via a rab5/phosphatidylinositol-3′-kinase–dependent machinery. Mol. Biol. Cell *17*, 3689–3704. https://doi.org/10.1091/mbc.e05-10-0980.

134. Hernandez-Valladares, M., Kim, T., Kannan, B., Tung, A., Aguda, A.H., Larsson, M., Cooper, J.A., and Robinson, R.C. (2010). Structural characterization of a capping protein interaction motif defines a family of actin filament regulators. Nat. Struct. Mol. Biol. *17*, 497–503. https://doi.org/10.1038/nsmb.1792.

135. Gerhard, D.S., Wagner, L., Feingold, E.A., Shenmen, C.M., Grouse, L.H., Schuler, G., Klein, S.L., Old, S., Rasooly, R., Good, P., et al.; MGC Project Team (2004). The status, quality, and expansion of the NIH full-length cDNA project: the mammalian gene collection (MGC). Genome Res. *14*, 2121–2127. https://doi.org/10.1101/gr.2596504.

136. Mortimer, R.K., and Johnston, J.R. (1986). Genealogy of principal strains of the yeast genetic stock center. Genetics *113*, 35–43. https://doi.org/10.1093/genetics/113.1.35.

137. Lee, S., Lim, W.A., and Thorn, K.S. (2013). Improved blue, green, and red fluorescent protein tagging vectors for S. cerevisiae. PLoS One *8*, e67902. https://doi.org/10.1371/journal.pone.0067902.

138. Sikorski, R.S., and Hieter, P. (1989). A system of shuttle vectors and yeast host strains designed for efficient manipulation of DNA in Saccharomyces cerevisiae. Genetics *122*, 19–27. https://doi.org/10.1093/genetics/122.1.19.

139. Brown, P.H., and Schuck, P. (2006). Macromolecular size-and-shape distributions by sedimentation velocity analytical ultracentrifugation. Biophys. J. *90*, 4651–4661. https://doi.org/10.1529/biophysj.106.081372.

140. Brautigam, C.A. (2015). Chapter five - calculations and publication-quality illustrations for analytical ultracentrifugation data. Methods in Enzymology (Academic Press). https://doi.org/10.1016/bs.mie.2015.05.001.

141. Laue, T.M., Shah, B., Ridgeway, T.M., and Pelletier, S.L. (1992). Computer-aided interpretation of sedimentation data for proteins. Analytical Ultracentrifugation in Biochemistry and Polymer Science (Royal Society of Chemistry). https://doi.org/10.1016/0169-2607(96)01719-1.

142. Noel, J.K., Levi, M., Raghunathan, M., Lammert, H., Hayes, R.L., Onuchic, J.N., and Whitford, P.C. (2016). Smog 2: a versatile software

package for generating structure-based models. PLoS Comput. Biol. *12*, e1004794. https://doi.org/10.1371/journal.pcbi.1004794.

143. Debye, P., and Huckel, E. (1923). The theory of electrolytes I. The lowering of the freezing point and related occurrences. Phys. Z. *24*, 185–206.

144. Berendsen, H.J.C., Vanderspoel, D., and Vandrunen, R. (1995). Gromacs - a message-passing parallel molecular-dynamics implementation. Comput. Phys. Commun. *91*, 43–56. https://doi.org/10.1016/0010-4655(95)00042-e.

145. Wood, C.W., and Woolfson, D.N. (2018). CCBuilder 2.0: powerful and accessible coiled-coil modeling. Protein Sci. *27*, 103–111. https://doi.org/10.1002/pro.3279.

146. Schrodinger, L. (2015). The PyMOL Molecular Graphics System Version 1.8. .

147. Ryan, V.H., Perdikari, T.M., Naik, M.T., Saueressig, C.F., Lins, J., Dignon, G.L., Mittal, J., Hart, A.C., and Fawzi, N.L. (2021). Tyrosine phosphorylation regulates hnRNPA2 granule protein partitioning and reduces neurodegeneration. EMBO J. *40*, e105001. https://doi.org/10.15252/embj.2020105001.

STAR★METHODS

KEY RESOURCES TABLE

REAGENT or RESOURCE	SOURCE	IDENTIFIER
Antibodies		
c-Myc Monoclonal Antibody (9E10)	N/A	N/A
PGK 1 Monoclonal Antibody	Invitrogen	Cat#459250; RRID: AB_2532235
IRDye® 800CW Goat anti-Mouse IgG Secondary Antibody	LI-COR	LIR 925-32210; RRID: AB_621842
Bacterial and virus strains		
Eschericchia coli	N/A	Rosetta (DE3)
Eschericchia coli	N/A	DH5α
Chemicals, peptides, and recombinant proteins		
DMEM, high glucose, GlutaMAX™ Supplement	Gibco	Cat#10566016
Fetal Bovine Serum, Research Grade Heat Inactivated	GE Hyclone	Cat#SV30160.03HI
Penicillin-Streptomycin (10,000 U/mL)	Gibco	Cat#15140122
Concanavalin A	Sigma	Product Number: L7647-100MG; CAS: 11028-71-0
Geneticin	Gibco	Cat#10131
herring sperm DNA	Promega	Cat#D1815
Lithium acetate dihydrate	Sigma	Product Number: L4158-250G; CAS: 6108-17-4
Poly(ethylene glycol),average mol wt 3,350	Sigma	Product Number: P4338-1KG; CAS: 25322-68-3
Yeast Nitrogen Base Without Amino Acids	Sigma	Product Number: Y0626-1KG
Raffinose	MP Biodmedicals	Cat#4010-032
Galactose	Sigma	Product Number: G0625-1KG; CAS: 59-23-4
Protease inhibitor cocktail IV	Bioworld	Cat#22020010-1
Trichloroacetic acid	Sigma	Product Number: T6399-250G; CAS: 76-03-9
Rabbit muscle acetone powder	Pel-Freez, LLC	Product code: 41995-2
Oregon Green™ 488 Iodoacetamide, mixed isomers	Invitrogen	Cat#O6010
NHS-dPEG®4-biotin	Sigma	Product Number: QBD10200-50MG
Uranyl acetate	Electron Microscopy Sciences	EMS Cat#22400; CAS: 541-09-3
Sulfuric acid	Sigma	Product Number: 258105-500ML-PC; CAS: 7664-93-9
mPEG-silane	Laysan Bio Inc	Lot#157-118
Biotin-PEG-saline	Laysan Bio Inc	Lot#154-174
Streptavidin	Sigma	Product Number: 11721666001
Glucose oxidase from *Aspergillus niger*	Sigma	Product Number: G7141-10KU; CAS: 9001-37-0
Methyl cellulose, viscosity 4,000CP	Sigma	Product Number: M0512-250G; CAS: 9004-67-5
Catalase from bovine liver	Sigma	Product Number: C40-100MG CAS: 9001-05-2
GelCode™ Blue Safe Protein Stain	Thermo Scientific™	Cat#24596

(*Continued on next page*)

Continued

REAGENT or RESOURCE	SOURCE	IDENTIFIER
Critical commercial assays		
ClonExpress II One Step Cloning Kit (50rxn)	Vazyme	Product serial number: C112-02
KAPA HiFi PCR Kit (250 U)	Roche	Cat#07958846001; Kit code: KK2202
PhantaMax Super-Fidelity DNA Polymerase	Vazyme	Product serial number: P505-d1
T4 DNA ligase	New England Biolabs	Cat#M0202S
Lipofectamine™ 3000 Transfection Reagent	Invitrogen	Cat#L3000001
Pierce™ BCA Protein Assay Kit	Thermo Scientific™	Cat#23227
Experimental models: Cell lines		
Mouse embryonic fibroblast	[133]	N/A
Experimental models: Organisms/strains		
S. cerevisiae: strain background: S288C	See Table S1	N/A
Oligonucleotides		
Primers	See Table S3	N/A
Recombinant DNA		
Plasmids	See Table S2	N/A
cDNA CORO1A	MGC	IMAGE ID: 5733853; Accession: BC110374.1; MGC: 117380
pSY5, pET21d (+) derived vector	[134]	N/A
PEGFP_N1 vector	Clontech	Cat#6085-1
pRS305 vector	ATCC	Cat#77140
pYeast Pro vector (pGAL-ORF-3× StreptagII-9×His)	[117]	N/A
Software and algorithms		
ImageJ	Open source	https://imagej.nih.gov/ij/
iTOL	Open source	https://itol.embl.de/
Deepcoill2	MPI Bioinformatics Toolkit	https://toolkit.tuebingen.mpg.de/tools/deepcoil2
Graphpad Prism 9	Graphpad Software	https://www.graphpad.com/scientific-software/prism/
Blastp	NCBI BLAST	https://blast.ncbi.nlm.nih.gov/Blast.cgi?PAGE=Proteins
Metamorph software	Molecular Devices, USA	https://www.moleculardevices.com/products/cellular-imaging-systems/acquisition-and-analysis-software/metamorph-microscopy
Chirascan	Applied Photophysics	https://www.photophysics.com/systems/chirascan-systems/chirascan/system-information/
SEDNTERP	BITC, University of New Hampshire	https://bitc.sr.unh.edu/index.php?title=Downloads
SEDFIT	Peter Schuck, NIH	http://www.analyticalultracentrifugation.com/sedfit.htm
GUSSI	Chad A. Brautigam, UT Southwestern MBR	https://www.utsouthwestern.edu/labs/mbr/software/
Huygens Essential	Scientific Volume Imaging	https://svi.nl/Huygens-Essential
IUPred2	Open source	https://iupred2a.elte.hu/
Common Tree	NCBI Taxonomy Tools	https://www.ncbi.nlm.nih.gov/Taxonomy/CommonTree/wwwcmt.cgi
SMOG2	Open source	https://www.smog-server.org/smog2/

(*Continued on next page*)

Continued		
REAGENT or RESOURCE	SOURCE	IDENTIFIER
Gromacs 5.1.2	Open source	http://www.gromacs.org/
Swiss-Pdb Viewer (aka DeepView)	SIB Swiss Institute of Bioinformatics	http://www.expasy.org/spdbv/
CCBuilder 2.0	Open source	http://coiledcoils.chm.bris.ac.uk/ccbuilder2/builder
PyMOL	Schrödinger	https://www.pymol.org/
Python for file processing	CWI, the Netherlands	https://www.python.org/
MATLAB vR2020b	The MathWorks, Natick, MA	https://www.mathworks.com/
PULCHRA	Open Source	http://cssb.bio.ogy.gatech.edu/skolnick/files/PULCHRA
Other		
Glass based dish, 27mm	Thermo Scientific™	Cat#150682
Microscope circular cover glass, thickness No.1.5, 25mm diameter	Marienfeld Superior, Germany	Cat#0112650
Microscope cover glass, thickness No.1.5 size: 24x50 mm	Marienfeld Superior, Germany	Cat#0102222
0.5mm Zirconia/Silica beads	Biospec Products	Cat#110791052
HisTrap HP column	Cytiva	Product No: 17524802
HiLoad 16/600 Superdex 200 pg column	Cytiva	Product No: 28989335
Superdex 200 Increase 10/300 GL column	Cytiva	Product No: 28990944
Amicon® Ultra-15 Centrifugal Filter Unit	Merk Millipore	Cat#UFC901024
HiPrep 16/60 Sephacryl S-300 HR column	Cytiva	Product No: 17116701
Carbon support film 200 Mesh, copper	Electron Microscopy Sciences	Cat#CF200-Cu
1mm path length cuvette	Hellma Analytics	Article No:100-1-40
TLA-100 Fixed-Angle Rotor	Beckman Coulter	343840
Plastic flow cell chamber (sticky-slide VI0.4)	Ibidi GmbH	Cat#80608

RESOURCE AVAILABILITY

Lead contact

Further information and requests for resources and reagents should be directed to and will be fulfilled by the lead contact Yansong Miao (yansongm@ntu.edu.sg).

Materials availability

Yeast strains and plasmids created in this study are available upon request from the lead contact.

Data and code availability

- All data reported in this paper will be shared by the lead contact upon request.
- This paper does not report original code.
- Any additional information required to reanalyze the data reported in this paper is available from the lead contact upon request.

EXPERIMENTAL MODEL AND STUDY PARTICIPANT DETAILS

Mouse embryonic fibroblasts

Mouse embryonic fibroblasts (MEFs) were a gift from Dr. Satyajit Mayor from the National Centre for Biological Sciences, Bangalore, India, and were used for Lipofectamine transfection.[133] Cells were grown in DMEM (high glucose, GlutaMAX™, Gibco) supplemented with 10% fetal bovine serum (GE HyClone), 100 units/ml penicillin and 100 μg/ml streptomycin at 37°C in a CO_2 incubator. To generate plasmids for overexpressing C-terminal GFP-tagged Coronin 1A full-length (pEGFP-N1-Coro1A-FL) and IDR truncation version (pEGFP-N1-Coro1A-ΔIDR) in MEFs, sequence encoding human Coronin1A was amplified by PCR using cDNA clone from Mammalian Gene Collection (MGC)[135] as template and inserted into the pEGF-N1 vector. The pEGFP-N1-Coro1A-ΔIDR plasmid was generated by deleting 401 aa-424 aa from full-length Coronin 1A. MEFs were transiently transfected with the plasmids described above using Lipofectamine 3000 (Invitrogen, USA) following the manufacturer's protocol and grown overnight on a round glass-bottom dish (Thermo Fisher) at 37°C in a CO_2 incubator for protein expression. Transfected cells were identified by GFP fluorescence under a microscope.

Saccharomyces cerevisiae strains

All yeast strains used in this study were derived from *S. cerevisiae* strain S288C[136] and are listed in Table S1.

For the spotting assay, strains were grown in YPD liquid medium (1% yeast extract, 2% peptone and 2% dextrose) at 25°C before plating on the YPD agar plate. For live-cell imaging, strains were grown in synthetic complete (SC) liquid medium with 2% dextrose without tryptophan at 30°C.

To construct plasmids for expressing mRuby2-tagged Crn1 full-length and truncation variants under native promoter in *S. cerevisiae*, pRS305-Crn1-FL-mRuby2-4*myc±500 plasmid was first generated by gene synthesis together with ClonExpress II (Vazyme Inc, China)-based cloning of sequences encoding full length Crn1, yeast-optimized mRuby2[137] and 4xMyc, plus 500 bp of upstream and downstream sequences of *CRN1*, which were inserted to integrating plasmid pRS305 in order,[138] truncated variants (pRS305-Crn1-ΔN-mRuby2-4*myc±500, pRS305-Crn1-ΔCC-mRuby2-4*myc±500, pRS305-Crn1-ΔIDR-mRuby2-4*myc±500, pRS305-Crn1-N-mRuby2-4*myc±500, pRS305-Crn1-IDR-mRuby2-4*myc±500, pRS305-Crn1-CC-mRuby2-4*myc±500, and pRS305-Crn1-ΔIDR-S-mRuby2-4*myc±500) were obtained by modifications on pRS305-Crn1-FL-mRuby2-4*myc±500 plasmid.

To express homo-oligomeric Crn1 variants, coding sequences of peptides including dimer, trimer, tetramer, and pentamer coiled-coils[70] were synthesized from Bio Basic (Bio Basic, Asia Pacific) and inserted at the original CC position of the pRS305-Crn1-ΔCC-mRuby2-4*myc±500 plasmid. The *Crn1Δ* strain YMY858 was obtained by replacing the *CRN1* ORF with the *Candida glabrata URA3* cassette in DDY904.[117] The pRS305-derived plasmids were integrated into the *LEU2* locus of strain YMY858 through XcmI digestion and lithium acetate transformation.[69] Briefly, YMY858 was cultured in YPD medium at 30°C overnight. The next day, it was reinoculated into a new medium with a starting optical density (OD_{600})=0.2 and cultured until OD=0.8–1. Ten-milliliter cultures were harvested by centrifugation for 10 min at 2000 x *g* at room temperature and washed once with sterile, double-distilled water. Yeasts were resuspended in 0.1 ml yeast transformation resuspension buffer (100 mM lithium acetate, 10 mM Tris, pH 8.0, 1 mM EDTA, pH 8.0) with 2–5 μg plasmids predigested by XcmI and 50 μg of herring sperm carrier DNA (Promega). Then, 700 μL of yeast transformation buffer (40% (w/v) polyethylene glycol, 100 mM lithium acetate, 10 mM Tris, pH 8.0, 1 mM EDTA, pH 8.0) was added and mixed well. The mixture was incubated at 30°C for 30 min followed by heat shock in a 42°C water bath for an additional 30 min. The mixture was centrifuged again for 5 min at 2000 x *g* to collect yeast cells, and cells were then resuspended with 200 μL sterile, double-distilled water and spread on a synthetic complete (SC) agar plate with 2% dextrose without leucine to select positive transformants. To introduce various *CRN1* variants into the *arc35-5* background, we crossed them with strain YXD160 (*crn1Δ arc35-5*, *derived from arc35-5*[74]), diploids were picked and induced to sporulate, tetrads were dissected and plated on YPD agar plates with 200 μg/ml Geneticin and SC agar plates with 2% dextrose without leucine to select target strains.

METHOD DETAILS

Yeast live-cell imaging

Yeast strains were cultured in SC liquid medium with 2% dextrose without tryptophan overnight and reinoculated into new medium to a starting OD_{600}=0.2. Cells were allowed to grow for an additional 4 hours before imaging. Cells were immobilized on concanavalin A (1 mg/ml, Sigma)-coated circular coverslips (Marienfeld Superior) and imaged at 25°C by a wide-field microscope Leica Dmi8 (Leica Microsystems) equipped with ORCA-Flash 4.0 LT scientific CMOS camera (Hamamatsu Photonics, Japan) and a Leica ×100 oil immersion objective lens (NA 1.4) using Metamorph software (Molecular Devices). Images were acquired as a z-axis stack with a step size of 0.25 μm for a total of 31 frames. Middle focal panel images were used for representatives and intensity analysis.

Yeast growth assay

For the yeast spotting assay, each strain was inoculated into YPD liquid medium and cultured at 25°C overnight. The next day, the culture was inoculated into fresh YPD medium with a starting OD_{600}=0.2 and cultured for an additional 3 hours. An additional reinoculation was performed starting from OD_{600}=0.2 and cultured for another 3 hours before being diluted to OD_{600}=0.1 for the spotting assay with tenfold serial dilutions in YPD medium. A 4 μL culture of each dilution was spotted on a YPD agar plate. Plates were incubated at the tested temperatures for 48 hours and scanned by a Perfection V600 Photo scanner (Epson) at 600 dpi. Images were converted to grayscale and inverted in Photoshop.

Yeast whole-cell extraction and immunoblotting

Yeast whole-cell protein extraction was prepared by trichloroacetic acid (TCA) precipitation. Yeasts were cultured in YPD liquid medium overnight at 30°C. Cells were reinoculated to OD_{600}=0.2 and cultured until OD_{600}=0.8-1. Ten OD cells were collected by centrifugation at 2000 x *g* for 10 min and washed once with sterile, double-distilled water. Cells were resuspended in 250 μL of 20% TCA (Sigma) solution with 100 μL 0.5 mm zirconia/silica beads (Biospec Products) and lysed by a Powerlyzer homogenizer (Qiagen) at 3500 rpm for 1 min, which was repeated 3 times with 5 min intervals on ice. The lysates were transferred out, and the beads were washed once with 300 μL of 5% TCA to collect the remaining lysates. An additional 700 μL of 5% TCA solution was added to the lysates to reach a final concentration of approximately 8% TCA. Samples were centrifuged at 14,000 x *g* for 10 min in an Eppendorf™ Benchtop Microcentrifuge (Thermo Fisher). Pelleted proteins were resuspended in 40 μL of 1 M Tris (pH 8.0) together with 80 μL of 2X sodium dodecyl sulfate (SDS) loading buffer (100 mM Tris, pH 6.8, 5% SDS, 20% glycerol, 0.1% bromophenol blue, and 200 mM DTT) and boiled at 95°C for 10 min. Samples were centrifuged again at 14,000 x *g* for 10 min, and supernatants were collected

for SDS–PAGE and western blot detection. Primary antibodies used for western blot: monoclonal mouse anti-pgk1 (22C5D8, Invitrogen) was diluted in TBST (20 mM Tris, pH 7.5, 150 mM NaCl, 0.1% v/v Tween 20) as 1:1000, monoclonal mouse anti-c-Myc (9E10, self-prepared) was diluted in TBST as 1:1000. The secondary antibody IRDye® 800CW goat anti-mouse (LI-COR) was diluted in TBST to 1:10,000. Blots were scanned by an Odyssey Infrared Imager (LI-COR Biosciences).

MEF live-cell imaging

To image the subcellular localization of GFP-fused Coronin 1A protein variants in MEFs, the culture medium was replaced by warm live-cell imaging solution (Invitrogen), and the culture conditions were maintained by a live-cell imaging chamber. Images were acquired on a spinning disk system (Gataca Systems) based on an inverted microscope (Ti2-E; Nikon) equipped with a sCMOS camera (Orca-Fusion; Hamamatsu), a confocal spinning head (W1; Yokogawa), and a 100x 1.45 NA Plan-Apo objective lens. Image acquisition was controlled by Metamorph software (Molecular Devices). Z-axis scanning images were acquired with a step size of 0.25 μm. An image of the middle focal plane was shown as a representative image. Images were deconvolved by Huygens Essential deconvolution software (Scientific Volume Imaging, Netherlands).

Protein expression and purification

A series of yeast Crn1 plasmids were constructed for protein expression and purification from *E. coli* Rosetta (DE3) using a pET-21d(+)(pSY5) vector that contains an 8x histidine tag and an HRV 3C protease cleavage site at the N-terminus of the protein of interest.[134] To generate pSY5-Crn1-FL, pSY5-Crn1-N, pSY5-Crn1-IDR, pSY5-Crn1-ΔN, and pSY5-Crn1-ΔCC plasmids, coding sequences of Crn1 1-651 aa, 1–400 aa, 401–604 aa, 401–651 aa, and 1–604 aa were amplified by PCR and inserted into the pSY5 backbone through T4 ligation. The pSY5-Crn1-ΔIDR plasmid containing 1–400 aa and 401–604 aa was generated from the pSY5-Crn1-FL plasmid, whereas the pSY5-Crn1-CC plasmid was generated by truncating 401–604 aa from the pSY5-Crn1-ΔN plasmid. The pSY5-Crn1-ΔIDR-S plasmid was generated by a two-step truncation that excluded 401–483 aa and 524–601 aa from the pSY5-Crn1-FL plasmid. Homo-oligomeric Crn1 constructs were obtained by inserting coding sequences of dimer, trimer, tetramer, and pentamer peptides[70] at the original CC position of the pSY5-Crn1-ΔCC plasmid.

To generate the pSY5-Crn1-IDR-50, pSY5-Crn1-IDR-100 and pSY5-Crn1-IDR-204 plasmids, DNA sequences encoding $(GS)_{25}$, $(GS)_{50}$ and $(GS)_{102}$ were synthesized from Azenta and inserted separately into the original IDR position of pSY5-Crn1-ΔIDR plasmid. The pSY5-Las17-polypVCA plasmid was constructed to express aa 300–633 aa of Las17.[77]

pSY5-based plasmids were transformed into *Escherichia coli* Rosetta (DE3) through 1.5 min of heat shock in a 42°C water bath, and bacteria were then spread on LB agar plates (1% tryptone, 0.5% yeast extract, 1% NaCl, and 1% agar) with 100 μg/ml ampicillin to select positive colonies. A single colony was picked to 20 mL of LB liquid medium and grown at 37°C overnight. The culture was scaled to 1 L in TB liquid medium (2.4% yeast extract, 2% tryptone, 0.4% glycerol, 0.017 M KH_2PO_4 and 0.072 M K_2HPO_4) with 100 μg/ml ampicillin and 35 μg/ml chloramphenicol. When the OD_{600} reached 1.5, expression was induced by 0.5 mM IPTG at 16°C overnight. Cells were harvested by centrifugation at 4°C and 5000 x *g* (rotor JA10, Beckman Coulter) and lysed by an LM20 microfluidizer (20000 psi) in binding buffer (50 mM Tris, pH 8.0, 500 mM NaCl, 20 mM imidazole) with 1 mM PMSF and protease inhibitor tablets (Thermo Fisher). Lysates were centrifuged at 20,000 x *g* and 4°C for 1 hour (JA 25.5 rotor, Beckman Coulter). The supernatant was kept and clarified by a 0.45 μM syringe filter (Pall Corporation) and then loaded onto a 5 mL Histrap column (Cytiva) connected to an FPLC AKTAxpress system (GE Healthcare). After affinity binding, the column was washed with binding buffer followed by gradient elution from 20 mM to 500 mM imidazole using elution buffer (50 mM Tris, pH 8.0, 500 mM NaCl, 500 mM imidazole). Peak fractions were checked by SDS–PAGE, and good fractions were combined and dialyzed in protein buffer (50 mM Tris, pH 8.0, 150 mM NaCl) overnight at 4°C. When necessary, the dialyzed protein solution was further separated by size exclusion chromatography using a HiLoad 16/600 Superdex 200 pg column (Cytiva) preequilibrated with protein buffer. Peak fractions were collected and checked by SDS–PAGE, and the fractions that passed the check were combined and concentrated with 10-kDa or 30-kDa cutoff concentrators (Merck Millipore). The protein concentration was measured with a BCA protein assay kit (Thermo Fisher). The protein solution was aliquoted into a small volume, frozen in liquid nitrogen and stored in a −80°C freezer.

Rabbit skeletal muscle actin (RMA) purification and labeling

To obtain monomeric ATP-bound RMA for the actin cosedimentation assay, transmission electron microscopy, and TIRF microscopy. Two grams of rabbit muscle acetone powder (Pel-Freez, LLC) was dissolved in 200 mL of cold G-buffer (2 mM Tris, pH 8.0, 0.2 mM ATP, 0.5 mM DTT and 0.1 mM $CaCl_2$) and stirred at 4°C overnight. The mixture was filtered with a cheese cloth to remove muscle powder, the actin-dissolved solution was further centrifuged at 2600 x *g* and 4°C (Type 45 Ti rotor, Beckman Coulter) for 30 min to collect the supernatant. Actin in the supernatant was then polymerized with slow stirring for 1 hour at 4°C by adding KCl and $MgCl_2$ solution to final concentrations of 50 mM and 2 mM, respectively. To remove tropomyosin and other actin-binding proteins, fine KCl powder was slowly added to reach a final concentration of 0.6 M, and the solution was stirred for another 30 min. The solution was then centrifuged at 14,000 x *g* (Type 45 Ti rotor, Beckman Coulter) for 3 hours at 4°C to collect the filamentous actin pellet. The pellet was then rinsed with cold G-buffer and homogenized with a homogenizer in 7 mL of cold G-buffer followed by a short sonication time. The sample was then dialyzed in 2 L G-buffer at 4°C for 48 hours to induce depolymerization (G-buffer was changed every 12 hours). After buffer exchange, the sample was centrifuged at 167,000 x *g* (SW 55 Ti swinging-bucket rotor, Beckman Coulter) at 4°C for 2.5 hours, and 5 mL of supernatant was collected and loaded onto a Sephacryl S-300 HR column

(GE healthcare) prebalanced with G-buffer. Peak fractions were collected and combined, and then 0.01% (final) sodium azide (Sigma) was added to inhibit fungal contamination and kept at 4°C. The actin concentration was measured by measuring the OD_{290} with a Nanodrop 2000 (Thermo Scientific).

To label actin with Oregon Green™ 488 iodoacetamide (Invitrogen) or NHS-dPEG®4-biotin (Sigma), the same steps were followed as RMA purification until pelleted filamentous actin was homogenized and sonicated. After this, the sample was dialyzed in 1 L G-buffer at 4°C overnight. The next day, the sample was changed to 1 L G-buffer without DTT and dialyzed for 4 hours at 4°C (buffer changed once). Oregon Green™ 488 iodoacetamide or NHS-dPEG®4-biotin was dissolved in dimethylformamide to a final concentration of 10 mM. Before labeling, the actin concentration was measured by reading the OD_{290} with a Nanodrop 2000 (Thermo Scientific). Actin was first diluted with an equal volume of cold 2X labeling buffer (50 mM imidazole, pH 7.5, 200 mM KCl, 0.6 mM ATP and 4 mM MgCl2) and further diluted to a final concentration of 23 μM with cold 1X labeling buffer. Then, a 10-fold molar excess of Oregon Green™ 488 iodoacetamide or NHS-dPEG®4-biotin was added dropwise while very gently vortexing. The mixture was covered with aluminum foil and rotated at 4°C overnight. The next morning, labeled filamentous actin was centrifuged at 167,000 x *g* (Type 50.2 rotor, Beckman Coulter) for 3 hours at 4°C. Pellets were collected and homogenized in 4 mL G-buffer, left on ice for 1 hour, and homogenized again. Actin was then dialyzed in 1 L G-buffer at 4°C for 48 hours to induce depolymerization (dark, G-buffer changed every 12 hours). After buffer exchange, actin was centrifuged at 436,000 x *g* (TLA100 rotor, Beckman Coulter) at 4°C for 1 hour. The supernatant was collected and further purified by a Sephacryl S-300 HR column (GE Healthcare) prebalanced with G-buffer. Peak fractions were collected and combined and then dialyzed in 500 mL G-buffer with 50% (v/v) glycerol at 4°C overnight to reduce volume. Small aliquots were frozen in liquid nitrogen and stored in a -80°C freezer.

Yeast protein expression and purification

To generate a plasmid for overexpression of the C-terminal 6xHis-tagged yCrn1-FL protein in budding yeasts, DNA sequences encoding full-length Crn1 were amplified using pRS305-Crn1-FL-mRuby2-4*myc±500 as a template and inserted into the pYeast Pro vector (pGAL-ORF-3×StreptagII-9×His).[117] Plasmids were transformed into strain YMY2043[117] using lithium acetate, and yeasts were spread on an SC agar plate with 2% dextrose without uracil to select positive transformants.

To obtain large-scale yeast culture for protein purification, we followed a published protocol.[69] Ten to 20 positive transformants were inoculated into 10 mL SC medium with 2% raffinose (MP biomedicals) without leucine and grown at 30°C with vigorous shaking for approximately 2 days until saturation (OD_{600} 2 to 3). Then, the saturated culture was scaled to 100 mL using SC medium with 2% raffinose without leucine and grown at 30°C with vigorous shaking until saturation again. The culture was then transferred to 1.9 L of fresh SC medium with 2% raffinose without leucine in a 5-L flask and kept growing at 30°C. When the culture reached saturation after 36 to 48 hours, 160 mL of 30% (w/v) galactose (Sigma) and 240 mL of 10X YP (10% w/v yeast extract, 20% w/v peptone) were added to the flask to a final concentration of 2% galactose and 1X YP, in which protein expression was induced for 12 to 16 hours with vigorous shaking at 30°C. Yeasts were collected by centrifugation at 6,000 x *g* (rotor JA10, Beckman Coulter) for 15 min at 4°C and washed twice with sterile double-distilled water. The cells were then resuspended in a 20% volume of sterile, double-distilled water, and the mixture was frozen into small balls by dripping into liquid nitrogen, which was further thoroughly ground by a Freezer/Mill 6870 cryomilling machine (SPEX SamplePrep) into a fine powder and stored at -80°C. For protein purification, 5 grams of yeast powder was dissolved in 30 mL binding buffer with 50 μL protease inhibitor cocktail IV (BioWorld), 300 μL of 100 mM PMSF, 75 μL of 0.2 M sodium orthovanadate (Sigma), 300 μL of 1 M glycerophosphate (Sigma) and 600 μL of 0.5 M NaF. The mixture was centrifuged at 20,000 x *g* (JA 25.5 rotor, Beckman Coulter) at 4°C for 1 hour. The supernatant was isolated and clarified by a 0.45 μm syringe filter (Pall Corporation). The filtered supernatant was loaded into a 5 mL Histrap column (Cytiva) connected to an FPLC AKTAxpress system (GE Healthcare). After affinity binding, the column was washed with binding buffer followed by gradient elution from 20 mM to 500 mM imidazole using elution buffer. Peak fractions were collected and checked by SDS–PAGE, and fractions were combined and dialyzed in 2 L protein buffer (50 mM Tris, pH 8.0, 150 mM NaCl) at 4°C overnight and then concentrated with 50-kDa cutoff concentrators (Merck Millipore). The protein concentration was measured by a BCA protein assay kit (Thermo Fisher). For storage, the protein was aliquoted into a small volume, frozen in liquid nitrogen, and stored in a −80°C freezer.

Specimen preparation and transmission electron microscopy

Purified RMA was polymerized for 1 hour in F-buffer (2 mM Tris, pH 8.0, 50 mM KCl, 1 mM $MgCl_2$, 1 mM EGTA, 0.2 mM ATP, 0.5 mM DTT, and 0.1 mM $CaCl_2$). 1 μM of each purified Crn1 protein variant was incubated with 2 μM prepolymerized F-actin for 30 min. Samples were then applied to a glow discharged carbon-coated copper grid (200 mess, Electron Microscopy Sciences) and incubated for 2 min. Extra volume was removed by filter paper, and grids were negatively stained with 1% uranyl acetate (Electron Microscopy Sciences) for 1 min. Grids were air-dried and examined at 120 kV by an FEI Tecnai 12 TEM equipped with an Ultrascan 1000 CCD camera (Gatan, Inc.).

Far-UV circular dichroism

Purified recombinant Crn1-CC and Crn1-IDR proteins were dialyzed against 50 mM sodium phosphate buffer (pH 7.4, 37.7 mM Na_2HPO_4, 12.3 mM NaH_2PO_4) at 4°C overnight. Protein was diluted to a final concentration within the optimal range for the detector. 300 μL of the sample was loaded into a 1 mm path length quartz cuvette (Hellma Analytics), and spectra were recorded on a Chirascan™ Circular Dichroism Spectrometer (Applied Photophysics) equipped with a temperature controller at 20°C and supplied

with constant N_2 flushing. Spectra were acquired from 260 nm to 190 nm (step size: 1 nm) with an integration time of 1 sec at each wavelength, and the baseline was corrected by a sample with buffer alone. Raw data in machine units θ (mdeg) were converted to mean residue ellipticity [θ] (degrees cm^2 $dmol^{-1}$ $residue^{-1}$) by the equation [θ] = θ x (0.1 x MRW)/(P x conc), where MRW=protein weight (daltons)/number of residues, P=patch length (cm) and conc=protein concentration (mg/ml).

Actin conversion assays

For the high-speed actin cosedimentation assay, a range of concentrations pre-assembled F-actin (0-12μM) was incubated in F-buffer with 1 μM Crn1 protein at room temperature for 30 min and then spun at 100,000 × *g* (high speed) with a TLA100 rotor (Beckman Coulter) for 25 min at 25°C. For the low-speed actin cosedimentation assay, a range of concentrations of Crn1 protein variants (0-8μM) was incubated in a buffer with physiological ionic strength (20 mM Tris, pH 8.0, 150 mM KCl, 1 mM $MgCl_2$, 1 mM EGTA, 0.2 mM ATP, 0.5 mM DTT, and 0.1 mM $CaCl_2$) with 2μM prepolymerized actin filaments at room temperature for 30 min and then spun at 10,000 × *g* (low speed) using an Eppendorf™ Benchtop Microcentrifuge (Thermo Fisher) for 30 min at 25°C. For both assays, equal volumes of supernatant and pellet fractions were collected and analyzed by SDS–PAGE and stained with GelCode™ Blue Stain Reagent (Thermo Fisher) overnight. Gels were imaged by a Perfection V600 Photo scanner (Epson), and densitometry of the band was quantified by ImageJ.

Total internal reflection fluorescence microscopy

The 24x50-mm glass coverslips (Marienfeld Superior) were cleaned by immersion in 20% sulfuric acid (Sigma) overnight and rinsed thoroughly with double-distilled water 3 times. Cleaned coverslips were then coated with 2 mg/ml methoxy-PEG-silane and 2 μg/ml biotin-PEG-saline (Laysan Bio Inc) in 80% ethanol (pH 2.0 with HCl) in a 70°C water bath overnight. The next day, the coverslips were rinsed thoroughly with double-distilled water and dried with a N_2 stream. Coated coverslips were covered with aluminum foil and stored at -80°C. Before experiments, a coated coverslip was stuck to the bottom side of a plastic flow cell chamber (Ibidi, sticky-slide VI0.4). Then, 30 μL of HBSA buffer (20 mM HEPES, pH 7.5, 1 mM EDTA, 50 mM KCl, and 1% bovine serum albumin) was pipetted into a cell and incubated for 1 min. Then, 30 μL of 0.1 mg/ml streptavidin in HEKG100 buffer (20 mM HEPES, pH 7.5, 1 mM EDTA, 50 mM KCl, and 10% (v/v) glycerol) was pipetted and incubated for an additional 1 min. Afterward, 30 μL of solution was pipetted out, and the cell was washed twice with 30 μL of 1X TIRF buffer (10 mM imidazole, pH 7.4, 50 mM KCl, 1 mM MgCl2, 1 mM EGTA, 0.3 mM ATP, 50 mM DTT, 15 mM glucose, 400 μg/ml glucose oxidase, 40 μg/ml catalase, and 0.5% methylcellulose [4000 cP]). Proteins were mixed with RMA (20% Oregon Green 488-labeled, 1% biotin-labeled) in G-buffer to the designated concentration, and 30 μL was pipetted into the cell followed by 30 μL of 2X TIRF buffer to initiate polymerization. To image Crn1-bundled actin filaments, a high salt 1X TIRF buffer with physiological ionic strength (10 mM imidazole, pH 7.4, 150 mM KCl, 1 mM MgCl2, 1 mM EGTA, 0.3 mM ATP, 50 mM DTT, 15 mM glucose, 400 μg/ml glucose oxidase, 40 μg/ml catalase, and 0.5% methylcellulose [4000 cP]) was used. Images were acquired as a stack at room temperature with 30-sec intervals for 15 min (for Arp2/3-mediated actin polymerization assay) or 5 min intervals for 90 min (for Crn1-mediated actin-bundling assay) using a Nikon Ti2-E inverted microscope equipped with a 100x 1.45NA Plan-Apo objective lens and a TIRF module (iLasV2 Ring TIRF, GATACA Systems) and an ORCA-Fusion sCMOS camera (Hamamatsu Photonics). Imaging lasers were provided by 405 nm/100 mW (Vortran), 488 nm/150 mW (Vortran), 561 nm/100 mW (Coherent) and 639 nm/150 mW (Vortran) combined in a laser launch (iLaunch, GATACA Systems). Focus was maintained by hardware autofocus (Perfect Focus System), and image acquisition was controlled by MetaMorph software (Molecular Device). For the Arp2/3-mediated actin polymerization assay, images were deconvolved by Huygens Essential deconvolution software (Scientific Volume Imaging, Netherlands) to diminish the background signal.

Analytical ultracentrifugation (AUC)

AUC Sedimentation Velocity (AUC-SV) experiments were performed on a Beckman Proteome Lab XL-I Analytical Ultracentrifuge using an 8-hole An-50 Ti analytical rotor. Samples were dialyzed overnight in physiological buffer (50 mM Tris, pH 8.0, 150 mM NaCl) and loaded into 2-sector cells fitted with a 1.2 cm epon centerpiece and quartz windows. The samples were centrifuged at 30,000 rpm or 45,000 rpm at 20°C, and absorbance at 280 nm (for Crn1-FL, Crn1-ΔCC, yCrn1-FL, Crn1ΔIDR-S, Crn1-IDR-50, Crn1-IDR-100 and Crn1-IDR-204) and 230 nm (for Crn1-CC, Crn1-IDR, and Crn1-ΔN) was recorded every 5-10 minutes during 15 hours of centrifugation. The data were analyzed with SEDFIT using *c(s)* and *c(s, ff_0)* size distribution models[139] and plotted with GUSSI[140]. Sedimentation coefficients were standardized to $s_{20,w}$ using the partial specific volume of the proteins (calculated using SEDFIT), solvent density, and viscosity (calculated using SEDNTERP)[141].

Coronin sequence analysis and the taxonomic tree

The murine Coronin 1A (NCBI accession NP_034028.1) N-terminal sequence (1-402 aa) was input as a query sequence to NCBI blastp against a nonredundant protein sequence database to identify coronin homologs for the 200 species that contain coronin family members, which were previously reported in[78]. We first excluded the hypothetical/unnamed/predicted/uncharacterized/putative candidate. In the remaining list of coronin candidates, we defined a cutoff for the "total alignment score" of 350, allowing us to identify the coronin homologs containing approximately the N-terminal 400 aa, which is the core and conserved coronin N-terminal domain. Therefore, we identified 392 coronin homologs from 200 species. For each identified coronin homolog, DeepCoil2 (https://toolkit.tuebingen.mpg.de/tools/deepcoil2)[54] was used to predict the coiled coil (CC) region, from which 11 (one from *B. bigemina*, one

from *P. berghei*, one from *P. chabaudi*, one from *P. knowlesi*, one from *P. reichenowi*, one from *P. Vivax*, one from *P. yoelii*, one from *T. annulate*, one from *A. aegypti*, and two from *M. lucifugus*) out of 392 coronin homologs do not have predicted CCs. Unique regions (IDRs) were identified between the N-terminus and CC, which were used to generate IDR-MAP. To build the taxonomic tree of the 200 species, the taxid of each species was input into the NCBI taxonomy tool-common tree, and the generated tree was modified by iTOL (https://itol.embl.de/).[81] The length of the predicted IDR was then integrated as a bar diagram outside the taxonomy tree, resulting in an IDR-MAP.

Coarse-grained simulation

Coarse-grained (CG) model

Our CG modeling approach follows Ravikumar et al.[129] In this CG model, each amino acid residue is represented by one CG bead at its Cα atom position, and the model contains both structure-based terms (i.e., Gō-like model terms) and statistical potential terms. The Gō-like model terms are used within a single chain to maintain the native structure. For the inter-chain interactions, we used a modified version of the Kim-Hummer (KH) model[130] based on the Miyazawa-Jernigan (MJ) statistical potential.[132] The potential energy function includes the interactions for bonds (E_{bond}), angles (E_{angle}), dihedral angles ($E_{dihedral}$), native-like contacts modeled by Lennard–Jones (LJ)-type potentials (E_{native}), electrostatic terms (E_{elec}) and hydrophobic terms (E_H) for the structured regions of the protein:

$$E = E_{bond} + E_{angle} + E_{dihedral} + E_{native} + E_{elec} + E_H$$

where $E_{bond} = \sum_{bonds} k_b(r - r_0)^2$, $E_{angle} = \sum_{angles} k_\theta(\theta - \theta_0)^2$ and $E_{dihedral} = \sum_{dihedrals}^{n=1,3} k_\Phi^{(n)}[1 + \cos(n(\Phi - \Phi_0))]$. The intrinsically disordered region (IDR, defined according to the sequence analysis above) neglects the angular and dihedral terms for flexibility. Here, r, θ and Φ are the instantaneous bond lengths, angles and dihedral angles, respectively, while r_0, θ_0, and Φ_0 are the corresponding values in the reference crystal structure. Force constants $k_b = 4.184 \times 10^4$ kJ/mol, $k_\theta = 8.368 \times 10\ kJ/mol \cdot rad$, $k_\Phi^{(1)} = 4.184\ kJ/mol$, and $k_\Phi^{(3)} = 2.092\ kJ/mol$.

The LJ-type potential energy function for native contacts is used between residue i and residue j as

$$E_{native} = \sum_{i,j} \varepsilon_0 \left[5\left(\frac{\sigma_{ij}^0}{r_{ij}}\right)^{12} - 6\left(\frac{\sigma_{ij}^0}{r_{ij}}\right)^{10} \right]$$

Where $\varepsilon_0 = 4.184 kJ/mol$, r_{ij} is the distance between residues *i* and *j*, and σ_{ij}^0 is the corresponding distance in the reference crystal structure. The native contact pairs are generated by SMOG2 software based on an atomistic structure.[142]

The electrostatic (E_{elec}) term is denoted as

$$E_{elec} = \sum_{i,j} \frac{q_i q_j}{4\pi D r_{ij}} e^{-\frac{r_{ij}}{k}}$$

Here, the electrostatic potential energy is treated through the Debye-Hückel method.[143] q_i represents the charge of residue *i*. The Debye screening length *k* equals 1 nm, corresponding to an ionic strength of approximately 100 mM, and the dielectric constant D equals 80 for the solvent medium (water). At pH 7.0, the residue charges $q_i = +1e$ for Lys and Arg, $q_i = -1e$ for Asp and Glu, and $q_i = +0.5e$ for His (*e* represents the elementary charge).

The hydrophobic interactions (E_H) are either attractive ($\varepsilon_{ij} < 0$) or repulsive ($\varepsilon_{ij} \geq 0$), where

$$\varepsilon_{ij} = \alpha\left(e_{ij}^{MJ} + \beta\right)$$

Here, e_{ij}^{MJ} is the Miyazawa-Jernigan (MJ) contact energy between residue *i* and residue *j*,[132] α is the parameter to scale E_H in relation to E_{elec}, and β (in the unit of RT, where R is the ideal gas constant and T represents temperature in Kelvin) is the parameter to balance the attractive and repulsive interactions.[129] Therefore, the hydrophobic interactions $E_H(i,j) = |\varepsilon_{ij}| \left[5\left(\frac{\sigma_{ij}}{r_{ij}}\right)^{12} - 6\left(\frac{\sigma_{ij}}{r_{ij}}\right)^{10} \right]$ if $\varepsilon_{ij} < 0$; $E_H(i,j) = \varepsilon_{ij}\left[5\left(\frac{\sigma_{ij}}{r_{ij}}\right)^{12} \left(1 - e^{-\left(\frac{r_{ij} - \sigma_{ij}}{d}\right)^2}\right) \right]$ if $\varepsilon_{ij} \geq 0$, where *d* is equal to 0.38 nm. Finally, a scaling factor γ is introduced for σ_{ij} as

$$\sigma_{ij} = \gamma(r_i + r_j)$$

where r_i is the van der Waals radius of residue *i*.[131]

Langevin dynamics (LD) simulation

The CG model was implemented for Langevin dynamics (LD) simulations with the GROMACS 5.1.2 package.[144] All simulations were carried out in the NVT ensemble (constant atom number, simulation box size, and temperature) at 300 K with a friction coefficient of 50/ps and a time step of 0.01 ps. Each simulation ran for at least 1000 ns for final analysis. The structures of IDRs were modeled by the software spdbv (http://www.expasy.org/spdbv/). The structure of the Crn1 coiled-coil domain was modeled by CCBuilder 2.0 (http://

coiledcoils.chm.bris.ac.uk/ccbuilder2/builder).[145] The structure of the Coronin1A coiled-coil domain was obtained from the Protein Data Bank (PDB ID: 2akf). Fusion of coiled-coil domains and IDRs and posing of each chain was performed by PyMOL[146] to generate the initial configuration for each simulation.

Data analysis

We used the potential energy per chain to evaluate the stability of different oligomers. Energy decomposition into electrostatic and hydrophobic interactions was further analyzed to determine the contribution. For a certain kind of species, e.g., murine Coronin1A coiled-coil (MmCC), its monomer was taken as the reference state whose potential energy per chain was shifted to zero.

All the contact maps followed the workflow demonstrated in Figure S5. We first calculated the contact probability for each pair of residues in the coiled-coil domain of two adjacent chains. Then, we mapped our protein sequences onto a known packing pattern of coiled coils to predict each whole motif (7 continuous residues in this case). We used a motif box, a 7×7 matrix (marked as a red square in Figure S5A), to show the contact probability between a certain pair of whole motifs on two adjacent chains. After that, we took the average among all the motif boxes to generate another 7×7 matrix, the motif-averaged contact map (Figures S5B and S5C), which represents the average contact probability between different pairs of motif sites. As all of the contact probability values are smaller than 0.5, the scale is set from 0 to 0.5 for better contrast. Following the approach of Ryan *et al.*[147] the interresidue distance cutoff for a contact to be formed is σ_{ij}, as defined in the coarse-grained model part. In addition to the motif-averaged probability map, the motif contact difference map (Figures 7F, 7G, and S5E) was constructed to present the contact probability differences at different contact pairs for two proteins (e.g., ScIDR-MmCC and MmCC in Figure S5D). The motif contact difference map showing differences in contact pattern between protein A and protein B is denoted as the "motif contact difference map (A minus B)". Finally, we used the Euclidean distance to measure the difference between two motif-averaged contact maps.

All the analyses were based on the last 500 ns of each simulation. GROMACS tools and MATLAB (v. R2020b; The MathWorks, Natick, MA) were used to analyze simulation trajectories. Figures of protein 3D structures were rendered by PyMOL.

QUANTIFICATION AND STATISTICAL ANALYSIS

mRuby2-patch intensity analysis

As illustrated in Figure S3A, to measure mRuby2 signal intensity at the actin patch, a rectangular box at 36x8 pixels was drawn crossing the Crn1-localized patches. The box was placed perpendicular to the mother cell membrane, with a patch in the middle. The cytosol region was defined by a proximal 8x8 box within the cell, the patch region was defined by an 8x8 box in the middle, and the background region was defined by a distal 8x8 box outside of the cell. The average intensity of each box was measured as the signal intensity, termed cytosol intensity (C), patch intensity (P), and background intensity (B). The patch-to-total ratio was calculated using the equation: (P-B)/[(P-B) +(C-B)].

Cortex enrichment analysis of Coronin 1A in MEFs

As illustrated in Figure S4H, to measure the cortex enrichment for GFP-fused Coro1A proteins in MEFs. A black line was drawn from the outside toward the cytoplasmic space, background (0–2.64 μm), cortex (3.3–6.6 μm) and cytosol (9.9–13.2 μm) regions were defined by the distance from the starting point. Mean gray value of each region was calculated, and cortex enrichment index was calculated by (cortex-background)/(cytosol-background).

Actin conversion analysis

The SDS–PAGE gel was scanned by the scanner and converted to an 8-bit gray value image in ImageJ. A rectangle area covering the entire band was selected, and area size and a mean gray value (mgv) were obtained from ImageJ, whereas a same-sized rectangle box from the background area was also selected for normalization. Band density was calculated as area x [(255-sample mgv) - (255-background mgv)]. In high-speed cosedimentation assay, the control was set as Crn1 alone without adding F-actin, which was used to exclude self-pelleting fraction. At each F-actin concentration, Crn1 band densities in both pellet and supernant were measured and summed as "Crn1 band density for 1 μM" , their averaged value was used as "total". Crn1 conc in pellet was calculated as (Crn1 band density-control band density)/total. Data points were curve fitted using the Hill equation in GraphPad Prism 9. To analyze actin bundling in the low-speed cosedimentation assay, both pellet and supernatant fractions of actin were used for analysis: at each Crn1 concentration, actin band densities from the pellet (P) and supernatant (S) were measured, and the percentage of actin in the pellet (%) was calculated as P/(P+S).

Statistical analysis

Statistical analyses were performed in GraphPad Prism 9, and an unpaired two-tailed Student's t-test assuming equal variances was used to determine the significance of difference between 2 groups. *p <0.05; **p < 0.01; ***p < 0.001; ****p < 0.0001; ns = not significant.